Research Square

Preprints are preliminary reports that have not undergone peer review.
They should not be considered conclusive, used to inform clinical practice,
or referenced by the media as validated information.

A Comparative Assessment of Pure AHP and Frequency Ratio-Based Hybrid Models for Landslide Susceptibility Mapping in the Ryesong River Basin, Democratic People's Republic of Korea

Hyon-Ryong Pang
phr198885@163.com

Kim Il-sung University
Ryong-Kil Ri
Kim Il-sung University
Chol-Ju Jang
Kim Il-sung University
Chung-Hyok Paek
Kim Il-sung University
Yun-Chol Choe
Kim Il-sung University
Kyong-Ho Jon
Kim Il-sung University
Hyok Ri
Kim Il-sung University

Research Article

Keywords: Expert-based model, Data-driven model, ROC-AUC, Bootstrap validation, Multicollinearity, Democratic People's Republic of Korea

Posted Date: June 11th, 2026

DOI: https://doi.org/10.21203/rs.3.rs-9960674/v1

License: This work is licensed under a Creative Commons Attribution 4.0 International License.
Read Full License

Additional Declarations: No competing interests reported.

A Comparative Assessment of Pure AHP and Frequency Ratio-Based Hybrid Models for Landslide Susceptibility Mapping in the Ryesong River Basin, Democratic People's Republic of Korea

Pang Hyon-Ryong[1]*, Ri Ryong-Kil[1], Jang Chol-Ju[1], Paek chung-Hyok[1], Choe Yun-Chol[2], Jon Kyong-Ho[3], Ri Hyok[1]

[1]Faculty of Resource Science, Kim Il Sung University, Pyongyang, Democratic People's Republic of Korea

[2]e-Libraly, Kim Il Sung University, Pyongyang, Democratic People's Republic of Korea

[3]Faculty of Physics, Kim Il Sung University, Pyongyang, Democratic People's Republic of Korea

*Corresponding author: Pang Hyon-Ryong

Email phr198885@163.com

ORCID:https://orcid.org/0009-0000-1234-9056

Contact number +8617833109452

Abstract

Landslide susceptibility mapping (LSM) is essential for hazard mitigation and land-use planning, yet the comparative performance of fully expert-driven, data-driven, and hybrid weighting schemes remains systematically underexplored. This study presents a controlled three-model comparison—the pure analytic hierarchy process (AHP), hybrid AHP-frequency ratio (AHP-FR), and hybrid AHP-normalized frequency ratio (AHP-NFR)—for a 1,071 km² Ryesong river basin spanning South Hwanghae Province, North Hwanghae Province and Kaesong city, Democratic People's Republic of Korea. Nine conditioning factors (slope, lithology, LULC, rainfall, elevation, distance to fault, aspect, curvature and distance to river) were derived from the ASTER DEM, Landsat 8 imagery, 1:200,000 geological maps, and meteorological records. An inventory of 86 landslide locations was partitioned into training (n=60) and validation (n=26) datasets. The factor weights were held constant across all the models via a single AHP pairwise comparison matrix (CR=0.083), whereas the class ratings were derived from (i) AHP subclass pairwise matrices (Pure AHP), (ii) raw frequency ratio values (AHP-FR), and (iii) probability-normalized FR values (AHP-NFR). Model performance was evaluated via receiver operating characteristic (ROC) curves, bootstrap confidence intervals (2000 iterations), spatial cross-validation, and landslide capture efficiency. The hybrid AHP-FR model achieved the highest prediction rate AUC (0.9127, 95% CI: 0.820–0.981), significantly outperforming both pure AHP (0.7988) and AHP-NFR (0.8624). Spatial cross-validation confirmed the robustness of AHP-FR with minimal performance degradation (1.4%). The AHP-FR hybrid concentrated 69.2% of the validation landslides within only 22.08% of the study area (capture efficiency ratio = 3.13). These results demonstrate that replacing subjective AHP class ratings with data-driven frequency ratio values—while retaining expert-derived factor weights—yields the optimal balance of predictive accuracy, spatial generalizability, and conservative high-susceptibility zone delineation for regional-scale landslide susceptibility assessment.

Keywords: Expert-based model; Data-driven model; ROC-AUC; Bootstrap validation; Multicollinearity; Democratic People's Republic of Korea

1. Introduction

Landslides represent one of the most destructive natural hazards worldwide, causing substantial loss of life, infrastructure damage, and economic disruption, particularly in mountainous regions with intense seasonal rainfall (Guzzetti et al. 1999; Corominas et al. 2014). The Democratic People's Republic of Korea (DPRK) experiences recurrent landslide events triggered by monsoon rainfall, complex geology, and steep topography, yet systematic landslide susceptibility mapping (LSM) for this region remains limited in the international literature. Accurate susceptibility assessment is a prerequisite for effective hazard mitigation, land-use planning, and early warning system development (Reichenbach et al. 2018; Roccati et al. 2021).

Landslide susceptibility assessment methods can be broadly categorized into three paradigms: knowledge-driven (expert-based), data-driven (statistical), and physically based deterministic approaches (Brenning 2005; Sachinthaka et al. 2025). Among knowledge-driven methods, the analytic hierarchy process (AHP), developed by Saaty (1980), has been widely adopted

for LSMs because of its structured framework for decomposing complex multicriteria decisions, its ability to incorporate diverse expert knowledge, and its transparent quantification of factor importance through pairwise comparisons (Dias and Gunathilake 2025; Kucuker 2025; Zighmi et al. 2025). However, pure AHP implementations—where both factor weights and intrafactor class ratings are derived from expert judgment—are inherently subjective and may not adequately capture the empirical relationship between conditioning factor classes and observed landslide occurrences (Panchal and Shrivastava 2021; Nath et al. 2024).

Conversely, the frequency ratio (FR) method is a purely data-driven bivariate statistical approach that derives class-level susceptibility directly from the spatial correlation between historical landslide locations and each factor class (Abdo 2022; Alam et al. 2025). While FR eliminates expert subjectivity at the class-rating level, its conventional implementation assigns equal weight to all conditioning factors, ignoring the established geotechnical principle that certain factors (e.g., slope angle) exert fundamentally stronger control on slope stability than others (e.g., aspect or curvature) do (Ozdemir and Altural 2013; Regmi et al. 2014).

These complementary strengths and weaknesses have motivated the development of hybrid models that integrate AHP-derived factor weights with FR-derived class ratings (Chandra et al. 2026; Das et al. 2026; Rebouh et al. 2026). The AHP-FR hybrid retains the expert's hierarchical structuring of factor importance while anchoring class-level susceptibility ratings in empirical landslide data. Despite the growing popularity of such hybrids, systematic comparisons that isolate the effect of class-rating methodology while holding factor weights constant remain scarce. Many studies compare AHP with FR as independent models (Melese et al. 2022; Alam et al. 2025), but few employ a controlled experimental design where identical factor weights are applied across pure AHP, raw FR, and normalized FR class-rating schemes (Yilmaz 2022; Hoa et al. 2023). Furthermore, robust validation frameworks incorporating bootstrap confidence intervals, spatial cross-validation, and capture efficiency metrics—recommended for establishing statistically defensible model superiority (Hosmer and Lemeshow 2000; Arabameri et al. 2020)—are rarely implemented comprehensively in AHP-FR comparative studies.

The present study addresses these gaps through a rigorous three-model comparative framework applied to a 1,071 km² landslide-prone region in the southwestern DPRK. The specific objectives are (i) to develop pure AHP, hybrid AHP-FR, and hybrid AHP-normalized FR (AHP-NFR) susceptibility models using identical AHP-derived factor weights (CR=0.083) but systematically varying class-rating methods; (ii) to validate model performance via ROC-AUC analysis, 95% bootstrap confidence intervals (2000 iterations), spatial cross-validation, and landslide capture efficiency ratios; and (iii) to identify the optimal weighting scheme that maximizes predictive accuracy while maintaining conservative and spatially generalizable susceptibility zonation for regional planning applications.

2. Study Area

The study area is located in the southwestern part of the Democratic People's Republic of Korea (DPRK), encompassing portions of South Hwanghae Province, North Hwanghae Province, and Kaesong city (Figure 1a). The area spans approximately 1,071 km² and is the main part of the Ryesong River basin, with geographic coordinates ranging from 126.24°E to 126.58°E longitude and 37.89°N to 38.24°N latitude (Figure 1b). This region was selected because of its relatively high landslide frequency in the DPRK, diverse geomorphological and geological conditions, and the availability of comprehensive geospatial data necessary for multifactor susceptibility modeling.

2.1 Topography and river system

The study area exhibits significant topographic relief, with elevations ranging from 0--750 m above sea level and slope angles varying from 0° to over 60° (Figure 1b). The Ryesong River, the primary drainage system, flows centrally through the study area in a northeast–southwest orientation and is structurally controlled by the Ryesong River Fault (Section 2.2). The western portion of the area is dominated by the Myoraksan Mountain range, while the Songaksan Mountain range defines the eastern topographic boundary. These mountainous zones, characterized by steep, highly dissected terrain, transition gradually into gently sloping piedmont surfaces and ultimately into broad alluvial plains toward the southwest. This diverse geomorphological setting—encompassing rugged mountains, incised river valleys, and low-relief depositional plains—creates spatially variable conditions highly conducive to landslide occurrence.

2.2 Geology

Tectonically, the study area lies within the Rimjin River Fold Belt (Paek et al. 1993), a structurally complex zone that preserves a geological record spanning from the Archean to the Holocene (Figure 1c). The stratigraphic succession comprises four major lithological groups:

Metamorphic rocks constitute the oldest formations and include the following:

- *Archeozoic Jangpung Group:* Predominantly augen gneiss, mylonitic gneiss, amphibolite, quartz-feldspathic gneiss, and quartzite. The strata strike NE 30–60° and dip 25–30° NW, reflecting regional compressional tectonics.
- *Proterozoic Rangrim Group:* Medium- to high-grade metamorphic rocks, including schists and gneisses, are extensively distributed in the northeastern sector.
- *Upper Proterozoic Jungsan Group:* Dominantly schists and quartzites, representing a transitional metamorphic–sedimentary sequence.

The sedimentary rocks are represented by the Saknyong Formation of the Paleozoic Rimjin Group. This unit consists mainly of dark gray phyllite and sandy phyllite and is widely distributed across the central and southern portions of the study area. The phyllitic composition renders these rocks particularly susceptible to weathering and strength degradation, making them a significant lithological control on landslide distribution.

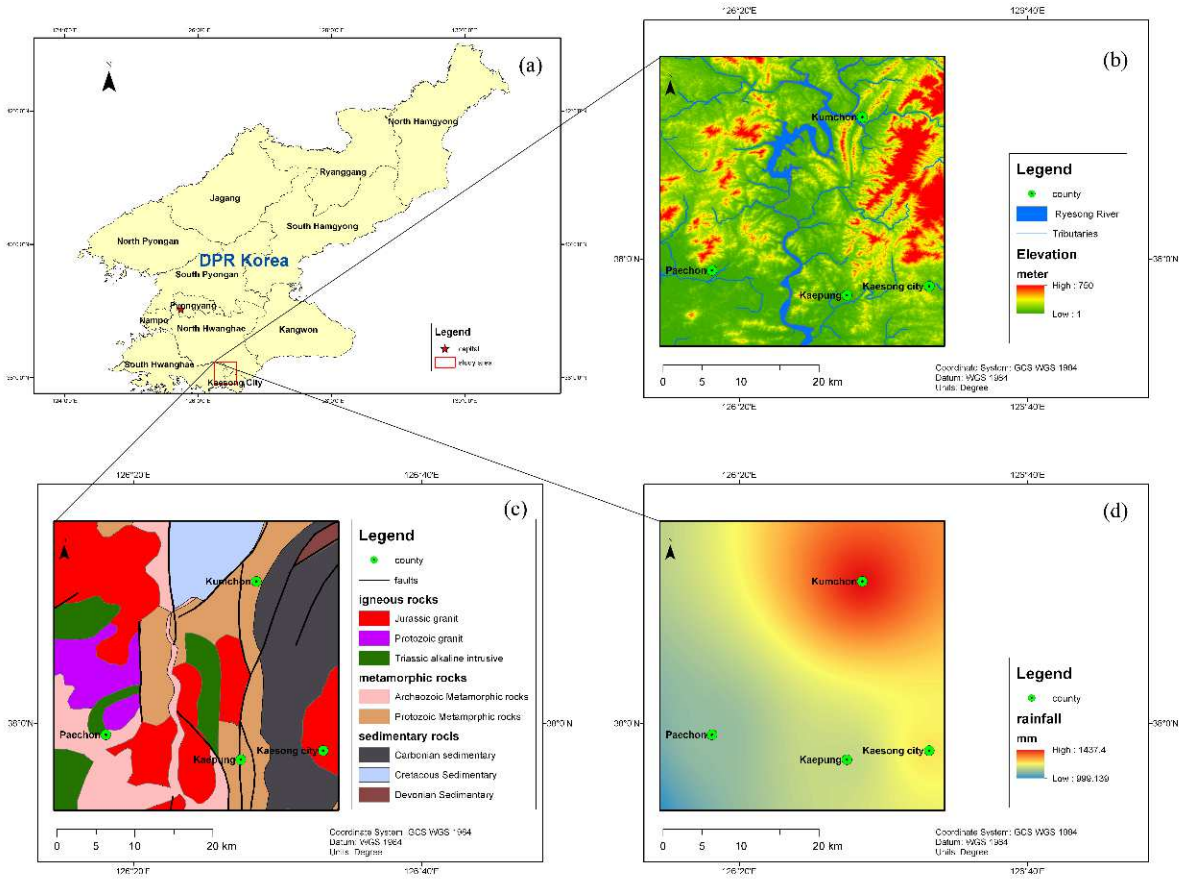


Figure 1. Overview of the study area: **(a)** geographical location; **(b)** topography; **(c)** geological map (modified from a 1:200,000 geological map sheet edited by the Central Geological Survey of Mineral Resources, Ministry of Natural Resources Development, DPR Korea, 1984); **(d)** mean annual rainfall distribution.

The intrusive rocks include the Proterozoic Ongjin Complex and the Mesozoic (Middle Jurassic) Danchon Complex. These predominantly granitic bodies form northwest–southeast-trending batholiths that intrude the older metamorphic and sedimentary sequences across extensive areas, particularly in the western and southeastern sectors.

Quaternary deposits, comprising fluvial sediments, alluvial sands, and gravels, dominate the southwestern plains along the lower reaches of the Ryesong River system. These unconsolidated deposits, while generally occupying low-relief terrain with limited landslide susceptibility, locally form steep riverbank scarps subject to lateral erosion-induced failure.

The study area is dissected by several major fault systems (Figure 1c). The most prominent fault is the Ryesong River Fault, a NE–SW-striking structure that parallels the course of the Ryesong River and is accompanied by numerous parallel and subsidiary faults. Additional fault systems striking N–S and NW–SE create a complex structural framework. These fault zones are associated with well-developed fracture networks where rocks exhibit intense brecciation, hydrothermal alteration, and deep weathering, substantially reducing their mechanical strength and increasing their permeability. The resulting zones of structural weakness serve as preferential pathways for groundwater infiltration and represent primary controls on the spatial distribution of landslides, as evidenced by the strong concentration of landslide events within 1,000 m of mapped fault traces (Section 4.3).

2.3 Climate and Precipitation

The study area experiences a humid continental climate with distinct seasonal variations driven by the East Asian monsoon system (Kim et al. 2025). The mean annual precipitation, derived from meteorological records spanning 2015–2024, ranges from 999 to 1,437 mm (data from the Meteorological and Hydrological Bureau, DPRK). Precipitation exhibited a pronounced spatial gradient, decreasing from northeast to southwest across the study area (Figure 1d), reflecting orographic enhancement along the northeastern mountain fronts and rain shadow effects in the southwestern lowlands.

The intra-annual distribution of precipitation is highly uneven. Approximately 40–50% of the annual precipitation (500–700 mm) occurs during the summer monsoon season (June–August), which is typically associated with intense, sustained rainfall events. This seasonal concentration of precipitation produces several conditions critical for landslide initiation: (i) progressive saturation of soil and weathered rock profiles; (ii) development of elevated pore water pressures at potential failure surfaces; (iii) reduction in the effective shear strength of slope materials through decreased matric suction; and (iv) increased surface runoff and fluvial erosion at slope toes. The coincidence of peak rainfall intensity with the period of maximum antecedent soil moisture creates conditions particularly favorable for widespread shallow landslide triggering.

The combination of steep, highly dissected topography (Section 2.1), structurally complex and variably weathered geology (Section 2.2), dense fault networks that facilitate deep weathering and groundwater percolation, and intense seasonal rainfall concentrated during the summer monsoon makes the study area highly susceptible to landslide occurrence and provides an ideal natural laboratory for comparative susceptibility modeling.

3. Materials and methods

The methodological framework of this study comprises five sequential stages, as illustrated in Figure 2:

Stage 1: Data acquisition. Relevant geospatial data were collected from multiple sources, including the ASTER DEM (30 m resolution) for topographic parameters, Landsat 8 imagery for land use/land cover classification, 1:200,000 geological maps for lithology and fault structures, and meteorological records (2015–2024) for rainfall distribution. A landslide inventory of 86 events was compiled through field surveys and aerial imagery interpretation and subsequently partitioned into training (n = 60) and independent validation (n = 26) datasets supplemented by 26 nonlandslide points.

Stage 2: Conditioning Factor Preparation. Nine conditioning factors were derived and classified: slope, lithology, LULC, rainfall, elevation, distance to fault, aspect, curvature, and distance to river. Each factor was rasterized at a 30 m resolution and classified into discrete classes on the basis of natural breaks and domain knowledge. Multicollinearity among factors was assessed via variance inflation factor (VIF) and tolerance (TOL) analyses.

Stage 3: Model development. Three distinct susceptibility models were constructed: (i) pure AHP, which employs expert-derived weights for both factors and classes via pairwise comparison matrices; (ii) hybrid AHP-FR, which combines AHP-derived factor weights with frequency ratio class ratings; and (iii) hybrid AHP-NFR, which uses probability-normalized FR values as class ratings while retaining AHP factor weights. The factor weights were held constant across all three models to isolate the effect of the class-rating methodology.

Stage 4: Susceptibility Classification. Landslide susceptibility index (LSI) values were calculated pixelwise by summing weighted factor contributions. The resulting continuous LSI maps were normalized to the [0,1] range via min–max normalization and then classified into five susceptibility zones (very low, low, moderate, high, very high) via the natural breaks (Jenks) classification method.

Stage 5: Model Validation. Model performance was evaluated via receiver operating characteristic (ROC) curve analysis with area under the curve (AUC) metrics. Statistical rigor was enhanced through bootstrap resampling (2,000 iterations) with 95% confidence intervals, spatial cross-validation under multiple resampling schemes, and quantification of landslide capture efficiency.

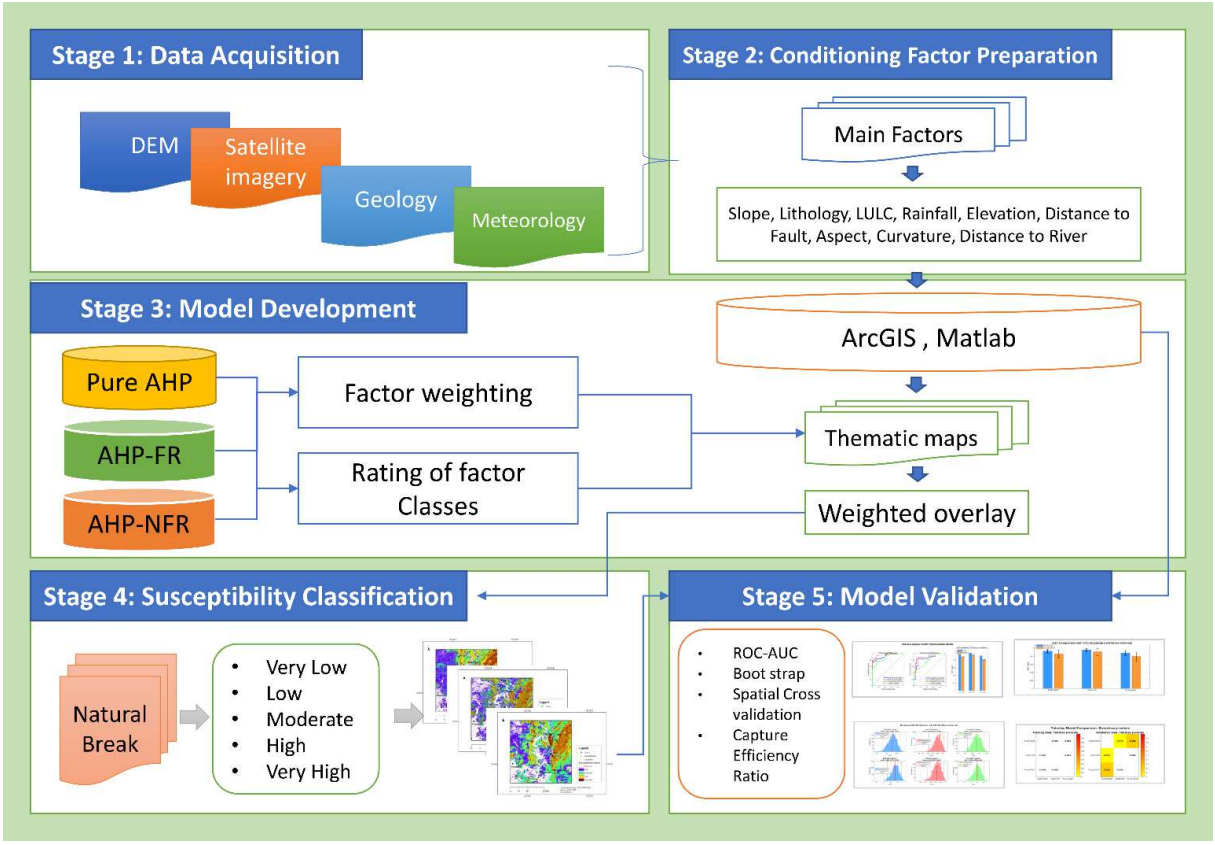


Figure 2 Technical workflow of the present study

3.1 Data collection and preparation

The landslide susceptibility map for the study area was developed using data from multiple sources, integrating satellite-derived information with existing geological, topographical, and environmental databases. The core methodological step involved creating individual thematic layers for each identified landslide conditioning factor.

On the basis of a thorough review of the relevant literature (Liu et al. 2024; Nath et al. 2024; Kucuker 2025; Zighmi et al. 2025) and the specific geoenvironmental characteristics of the study area, nine conditioning factors were selected as predictors for landslide susceptibility mapping. These factors encompass four major categories: topographic (slope, aspect, elevation,

curvature), hydrological (rainfall, distance to river), geological (lithology, distance to fault), and anthropogenic/land cover (LULC). The selection criteria prioritized factors that are (i) physically relevant to landslide occurrence on the basis of established geotechnical principles; (ii) available across the entire study area at adequate spatial resolution; and (iii) commonly employed in comparable LSM studies to ensure result comparability.

The data were compiled from multiple sources, as detailed in Table 1. Preexisting analog maps (e.g., lithology and faults) were scanned, georeferenced, rectified, and digitized in ArcGIS 10.7.1. The remotely sensed data included Landsat 8 imagery (NASA's EOSDIS) and a 30 m resolution ASTER Global Digital Elevation Model (DEM). The DEM served as the foundational dataset for deriving key topographic variables—slope, aspect, curvature, and elevation—via spatial analyst tools.

Ten years of annual rainfall records (2015–2024) from six local meteorological stations (Kumchon, Jangpung, Yonan, Peachon, Kaepung, and Kaesong) were used to derive the mean annual precipitation data. The point rainfall measurements were interpolated into a continuous surface across the study area via the inverse distance weighting (IDW) method with a power parameter of 2, which was selected to balance local fidelity with regional smoothness. Finally, all nine factors were standardized and converted into thematically aligned raster layers at 30 m resolution for subsequent susceptibility modeling.

Table 1. Summary of the nine conditioning factors.

Factor	Type	Range	Data Source	Resolution
Slope	Continuous	0–60°	DEM (ASTER GLOBAL)	30 m
Rainfall	Continuous	999–1,437 mm	Meteorological stations (IDW interpolation)	30 m
Elevation	Continuous	0–750 m	DEM (ASTER GLOBAL)	30 m
Distance to Fault	Continuous	0–11,757 m	Geological map (1:200,000 from Geological Survey of the DPRK) + Euclidean distance	30 m
Distance to River	Continuous	95–3,936 m	DEM (ASTER GLOBAL), Topographic map + Euclidean distance	30 m
Aspect	Circular (0–360°, converted to 1–9 classes)	1–9	DEM (ASTER GLOBAL)	30 m
Curvature	Continuous	−17.225~ 16.85	DEM (ASTER GLOBAL)	30 m
Lithology	Categorical	1–4	Geological map (1:200,000 from Geological Survey of the DPRK)	Vector
LULC	Categorical	1–6	Landsat 8 OLI (2022)	30 m

3.1.1 Landslide Inventory

The landslide inventory was compiled through systematic field surveys conducted between 2018 and 2023, supplemented by interpretation of high-resolution satellite imagery. A total of 86 landslide locations were identified and mapped as point vectors. For each landslide site, field observation records were documented, including in situ photographs, morphological characteristics, and classification of slide types (shallow translational slides, rotational slumps, debris flows, and rockfalls). This field-based approach ensures the reliability of the inventory for both model training and independent validation.

For susceptibility modeling, the inventory was randomly partitioned into a training dataset (n = 60, 70%) and a validation dataset (n = 26, 30%). The training dataset was used to calculate frequency ratio values (Section 3.3.1) and construct the success rate ROC curves, whereas the validation dataset was reserved exclusively for independent prediction rate assessment and capture efficiency analysis.

To enable binary classification performance evaluation, 86 nonlandslide points were generated via a buffer sampling method. A 100 m buffer was created around each of the 86 landslide points to define exclusion zones, preventing the sampling of nonlandslide points from transitional or marginally stable areas adjacent to known failures. Stable areas were identified as locations satisfying two criteria: slope angle < 10° and land use classes of grassland, forest, or farmland (excluding water bodies, swamps, and settlements). Nonlandslide points were randomly sampled from these stable areas and confirmed through satellite imagery interpretation to ensure the absence of visible landslide features. The spatial distributions of the training and validation points (including both historical landslides and nonlandslides extracted from stable areas) are shown in Figure 3.

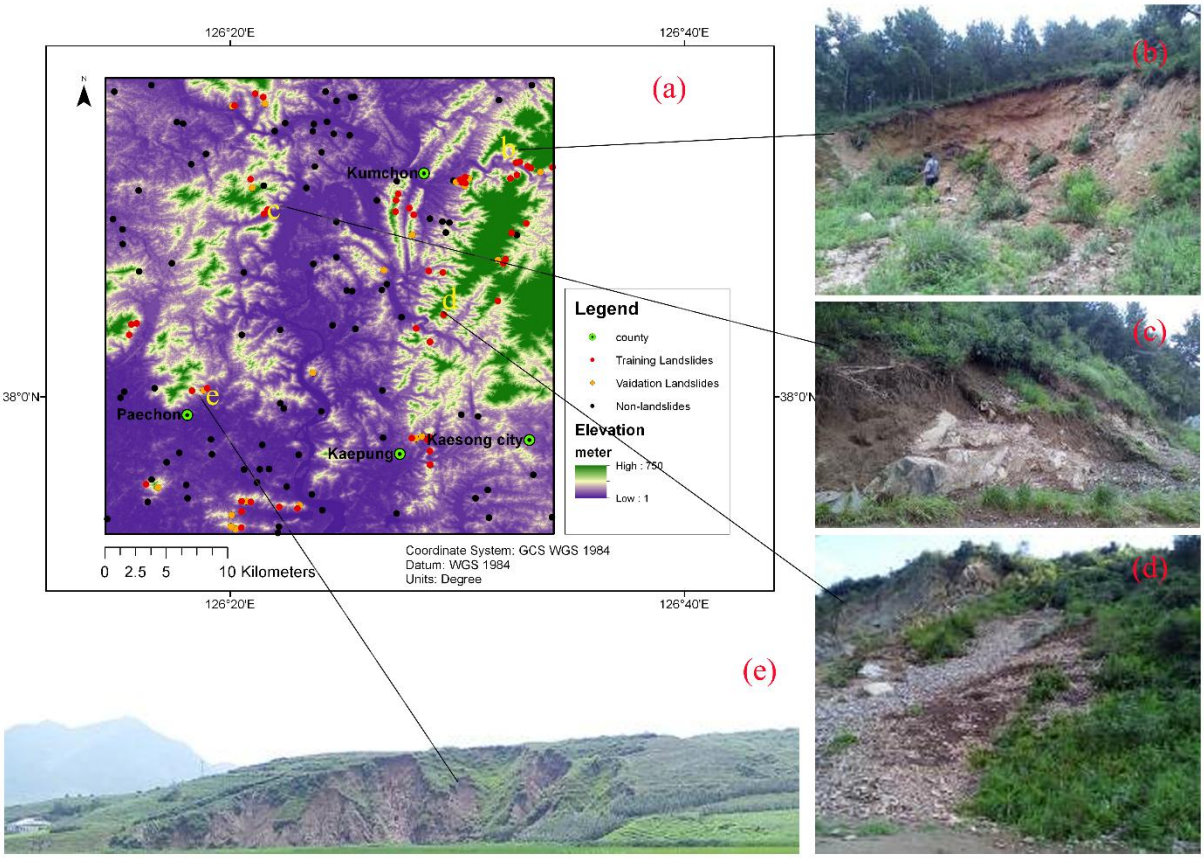


Figure 3 Landslide inventory of the study area and the distribution of training and validation points

3.1.2 Multicollinearity analysis

Before model development, a multicollinearity analysis was conducted to ensure the independence of the selected conditioning factors. Multicollinearity occurs when two or more predictor variables are highly correlated, which can lead to unstable coefficient estimates, inflated standard errors, and reduced model interpretability, particularly in regression-based and weighted linear combination approaches (Wooldridge 2015; Chatterjee and Simonoff 2013; Selamat et al. 2025). Although the AHP and FR methods employed in this study are not regression-based, assessing factor independence remains important because redundant factors can effectively double-count the same terrain characteristics, artificially inflating or distorting susceptibility estimates.

Multicollinearity was assessed via two complementary approaches:

Pearson's correlation matrix. Bivariate correlation coefficients (r) were computed for all pairs of the nine conditioning factors via continuous data extracted at the 120 training points (60 landslides, 60 nonlandslides). Pearson's r ranges from −1 (perfect negative correlation) to +1 (perfect positive correlation), with values approaching these extremes indicating strong linear dependence between factor pairs. Figure 4 shows the Pearson's correlation matrix of the nine conditioning factors. The color scale ranges from blue (negative correlation) through white (no correlation) to red (positive correlation), with color saturation proportional to correlation strength. Correlation coefficients are displayed in each cell. The strongest positive correlations are observed between elevation and slope ($r = 0.72$) and between LULC and elevation ($r = 0.65$), reflecting the topographic control on land cover distribution. The strongest negative correlations involve lithology with rainfall ($r = -0.63$) and elevation ($r = -0.51$), reflecting the spatial segregation of rock types along climatic and topographic gradients. Most pairwise correlations fall below $|r| = 0.50$, and all remain below $|r| = 0.72$, confirming the absence of critically strong linear dependencies that would preclude the joint use of any factor pair.

Variance inflation factor (VIF) and tolerance (TOL). While Pearson's correlation effectively detects pairwise linear relationships, it does not capture multivariate collinearity where a factor is jointly predicted by a combination of several other factors. The variance inflation factor (VIF) and tolerance (TOL) address this limitation by quantifying how much the variance of a regression coefficient is inflated because of correlations with all other predictors simultaneously. The VIF and TOL were calculated via the same 120 training points, with TOL defined as the reciprocal of the VIF:

$$VIF = 1/(1 - R_j^2) \quad (1)$$

$$\text{TOL} = 1/VIF \quad (2)$$

where R_j^2 is the coefficient of determination from regressing the *j*-th predictor against all other predictors.

The interpretation thresholds adopted in this study follow established guidelines (Wooldridge 2015; Chatterjee and Simonoff 2013):

- VIF < 5 or TOL > 0.2: Low multicollinearity (acceptable for model inclusion)
- 5 ≤ VIF < 10 or 0.1 < TOL ≤ 0.2: Moderate multicollinearity (caution warranted)
- VIF ≥ 10 or TOL ≤ 0.1: High multicollinearity (problematic; factor removal recommended)

For the three categorical factors (lithology, LULC, and aspect), the class codes (e.g., lithology classes 1–4; LULC classes 1–6; aspect classes 1–9) were treated as continuous integer variables in the regression that underlies the variance inflation factor (VIF) calculation. This practical simplification is commonly adopted in the multicollinearity screening of landslide conditioning factors when no severe collinearity is detected (e.g., Achu et al. 2022; Youssef and Pourghasemi 2020). The very low VIF values obtained (all below 3.2) indicate that, even under this linear approximation, the categorical factors do not introduce problematic dependencies with the other predictors.

Table 2 summarizes the VIF and tolerance results. All the VIF values were substantially below the critical threshold of 5, ranging from 1.14 (curvature) to 3.13 (elevation), with a mean VIF of 1.87. All tolerance values exceeded 0.2, ranging from 0.320 to 0.877. The factor with the highest VIF, elevation (3.13), shows a moderate correlation with slope and rainfall—physically consistent relationships reflecting orographic precipitation effects and the concentration of steep terrain at intermediate elevations. However, the VIF remains well within the acceptable range, confirming that no factor introduces problematic redundancy.

Table 2. Multicollinearity analysis results.

Factor	VIF	Tolerance (TOL)	Multicollinearity Level
Slope	2.61	0.384	Low (acceptable)
Rainfall	2.36	0.424	Low (acceptable)
Elevation	3.13	0.320	Low (acceptable)
Distance to Fault	1.65	0.607	Low (acceptable)
Distance to River	1.31	0.763	Low (acceptable)
Aspect	1.24	0.804	Low (acceptable)
Curvature	1.14	0.877	Low (acceptable)
Lithology	2.23	0.448	Low (acceptable)
LULC	1.94	0.516	Low (acceptable)

The convergence of evidence from both Pearson's correlation matrix (Figure 4) and the VIF/TOL analysis (Table 2) provides strong support for factor independence. The correlation heatmap visually confirms the absence of strong pairwise linear relationships, whereas the VIF diagnostics verify that no factor is substantially predicted by multivariate combinations of other factors. These complementary results indicate no significant multicollinearity among the nine conditioning factors, confirming that all variables can be safely retained for subsequent susceptibility modeling without concern for variance inflation or double-counting bias.

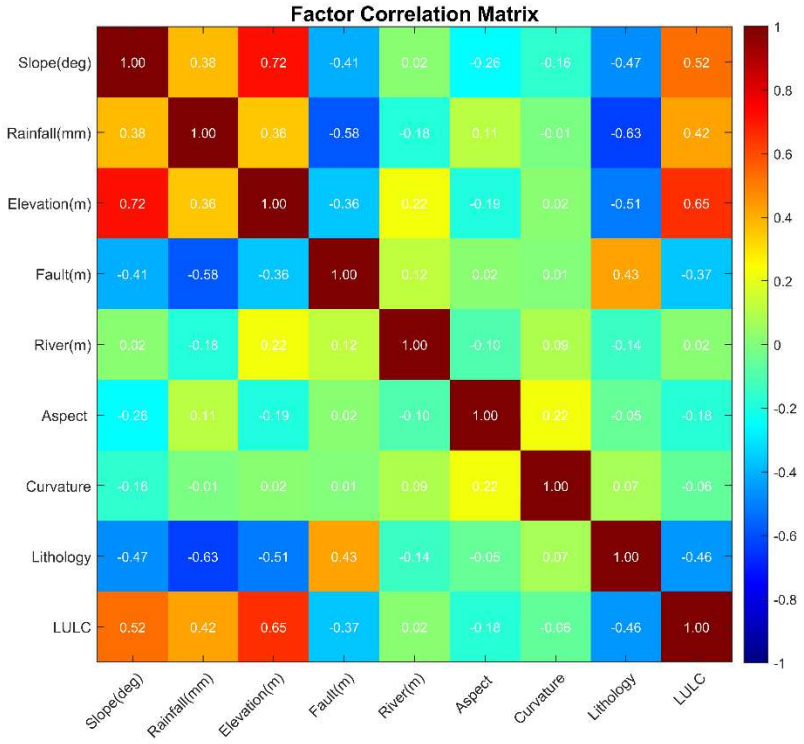


Figure 4 Pearson's correlation matrix of the nine conditioning factors.

3.2 Analytic Hierarchy Process (AHP)

The analytic hierarchy process (AHP), developed by Saaty (1980), is a semiquantitative multicriteria decision-making (MCDM) method designed to decompose complex decisions into hierarchical structures and derive priority weights through systematic pairwise comparisons. In the context of landslide susceptibility mapping, the AHP enables the structured integration of expert knowledge to assign relative importance weights to conditioning factors on the basis of their perceived influence on slope failure occurrence (Dias and Gunathilake 2025; Panchal and Shrivastava 2021). The method is particularly suited to geohazard applications where empirical data may be limited or where a mechanistic understanding of factor interactions informs expert judgment (Islam et al. 2025; Chandra et al. 2026). A key advantage of the AHP is its explicit accommodation of minor judgment inconsistencies through consistency ratio diagnostic, ensuring that derived weights maintain logical coherence without requiring perfect transitivity (Chaiyaphan and Ransikarbum 2020).

The AHP implementation in this study follows the standard four-step procedure (Saaty and Vargas 2001):

Step 1: Problem decomposition. The complex, unstructured problem of landslide susceptibility assessment is decomposed into a hierarchical structure comprising the overall goal (landslide susceptibility), the decision criteria (nine conditioning factors), and, where applicable, subcriteria (discrete classes within each factor).

Step 2: Hierarchical structuring. The nine conditioning factors are organized according to their causal relationships with slope instability and grouped into four thematic categories (topographic, hydrological, geological, and land cover) to facilitate systematic pairwise comparisons.

Step 3: Pairwise comparison and numerical judgment. The relative importance of factors is determined through pairwise comparisons via Saaty's fundamental scale of absolute numbers (Table 3). This scale ranges from 1 (equal importance) to 9 (extreme importance), with intermediate values (2, 4, 6, 8) representing compromise judgments. The assignment of importance values was informed by analysis of the landslide inventory, field observations of failure mechanisms, and a comprehensive literature review (Liu et al. 2024).

Step 4: Priority derivation and consistency verification. Numerical weights are derived from the pairwise comparison matrix via the eigenvector method, and judgment consistency is evaluated via the consistency ratio (CR), with CR < 0.10 indicating acceptable logical coherence.

Table 3 Standard AHP scale for paired comparisons (Saaty 1977).

Intensity of Importance	Definition	Explanation
1	Equal importance	Two factors contribute equally to the objective
3	Moderate importance	Experience and judgment slightly favor one factor over another
5	Strong importance	Experience and judgment strongly favor one factor
7	Very strong importance	A factor is favored very strongly; its dominance is demonstrated in practice
9	Extreme importance	The evidence favoring one factor over another is of the highest possible order of affirmation
2, 4, 6, 8	Intermediate values	Used to represent compromise between adjacent judgments
Reciprocals	Inverse comparison	If factor i has one of the above values assigned compared to factor j, then j has the reciprocal value compared to i

3.2.1 Pairwise comparison matrix construction

For n conditioning factors, the pairwise comparison yields a square matrix $A = (a_{ij})$ of order n, where a_{ij} represents the relative importance of factor i compared with factor j. The matrix satisfies the reciprocity condition $a_{ji} = 1/a_{ij}$ for all i, j, and the identity condition $a_{ii} = 1$ for all diagonal elements:

$$A = \begin{pmatrix} 1 & a_{12} & \cdots & a_{1n} \\ \frac{1}{a_{12}} & 1 & \cdots & a_{2n} \\ \vdots & \vdots & \vdots & \vdots \\ \frac{1}{a_{1n}} & \frac{1}{a_{2n}} & \cdots & 1 \end{pmatrix} \quad (3)$$

The pairwise comparison matrix for the nine conditioning factors, together with the derived weights, is presented in Table 5 (Section 4.2).

3.2.2 Weight Calculation

Following construction of the pairwise comparison matrix, the vector of relative weights $w = [w_1, w_2, w_3..., w_n]$ is computed via Saaty's eigenvector method. The procedure involves two steps:

First, the matrix is normalized by dividing each element by the sum of its column, ensuring that all columns sum to unity:

$$N_{ij} = \frac{a_{ij}}{\sum_{i=1}^{n} a_{ij}} \quad (4)$$

where N_{ij} represents the normalized element corresponding to a_{ij}.

Second, the weight for each factor is calculated as the rowwise average of the normalized matrix:

$$w_i = \frac{\sum_{j=1}^{n} N_{ij}}{n} \quad (5)$$

The resulting weights (Table 6, Section 4.2) sum to 1.0 and represent the relative contribution of each factor to landslide susceptibility as judged by expert evaluation.

3.2.3 Consistency Verification

Human judgment is inherently subject to minor inconsistencies, particularly when multiple factors are compared simultaneously. The AHP explicitly accommodates this through the consistency ratio (CR), which quantifies the degree of logical coherence in pairwise judgments. The CR is derived through a two-step calculation:

First, the consistency index (CI) is computed from the principal eigenvalue λ_{max} of the pairwise comparison matrix:

$$CI = \frac{\lambda_{max} - n}{n-1} \qquad (6)$$

where n is the number of factors compared. For a perfectly consistent matrix, $\lambda_{max} = n$ and CI = 0.

Second, the CR is obtained by normalizing the CI against the random index (RI), which represents the average consistency index expected from randomly generated reciprocal matrices of the same order:

$$CR = \frac{CI}{RI} \qquad (7)$$

The RI values for matrices of various sizes are provided in Table 4 (Saaty 1990). For the present study, with n = 9 factors, RI = 1.45.

Table 4 Random consistency indices (RIs) for matrices of various sizes (Saaty 1990).

n	1	2	3	4	5	6	7	8	9	10	11	12
RI	0.00	0.00	0.50	0.90	1.12	1.24	1.32	1.41	1.45	1.49	1.51	1.53

A CR value below 0.10 (10%) indicates that the pairwise judgments exhibit acceptable consistency and that the derived weights are reliable for subsequent analysis (Saaty 1990). Higher CR values suggest significant judgment inconsistencies that warrant matrix revision. For the present study, CR = 0.083 (Table 6), confirming the logical coherence of the expert judgments.

3.2.4 Subclass weighting for the pure AHP model

In the pure AHP model (Model 1), both factor-level weights and class-level ratings are derived exclusively through expert judgment. While the factor weights (Section 3.2.2) establish the relative importance among conditioning factors, the class ratings quantify the relative susceptibility of individual classes within each factor. For each of the nine factors, a separate pairwise comparison matrix was constructed to compare the discrete classes of that factor using the same Saaty 1–9 scale (Table 3) and the eigenvector calculation procedure described above.

For example, the slope factor (five classes: 0–10°, 10–20°, 20–30°, 30–40°, >40°) required a 5 × 5 pairwise comparison matrix where steeper classes were judged to have progressively higher susceptibility on the basis of the established geotechnical principle that an increased slope angle elevates gravitational driving stress. The resulting class priority vectors, normalized to sum to unity within each factor, serve as the class ratings (R_{ij}) in the pure AHP landslide susceptibility index calculation. The complete set of subclass pairwise matrices and derived ratings for all nine factors is presented in Table 6 (Section 4.2), with all CR values below 0.10, confirming judgment consistency at the subclass level.

3.3 Frequency ratio (FR) and hybrid models

3.3.1 Pure frequency ratio (FR) model

The frequency ratio (FR) method is a bivariate statistical approach that quantifies the spatial correlation between landslide occurrence and each class of a conditioning factor (Panchal and Shrivastava 2021; Alam et al. 2025). The FR approach is purely data driven, eliminating expert subjectivity by deriving weights directly from the observed spatial distribution of landslide points. For each factor class i of factor j, the FR is calculated as:

$$FR_{ij} = (NLS_{ij} / NLS_{total}) / (Npix_{ij} / Npix_{total}) \quad (8)$$

where:

- NLS_{ij}= number of landslide points in class i of factor j

- NLS_{total}= total number of landslide points in the training dataset (n = 60)

- $Npix_{ij}$ = number of pixels in class i of factor j within the study area

- $Npix_{total}$= total number of pixels in the study area

A FR > 1 indicates a greater correlation than expected by chance. The FR analysis was performed using the 60 training landslide points. The calculated FR values for all the factor classes are presented in Table 7.

The landslide susceptibility index (LSI) is calculated by summing the Fr values for each subfactor (Panchal and Shrivastava, 2021; Alam et al., 2025; Das et al., 2026):

$$LSI = \sum_{i=1}^{n} FR_i \quad (9)$$

where FR is the frequency ratio and n is the number of causative factors. This formula treats every conditioning factor as equally important because the FR values of all factor classes are simply summed without weighting the factors themselves. This is an unweighted linear combination, which implies that, *a priori*, slope steepness contributes equally to susceptibility as, for example, distance to a river. While this approach has been widely applied and often yields satisfactory results (Panchal and Shrivastava, 2021; Alam et al., 2025; Das et al., 2026), it does not allow one factor to exert a stronger influence on the final susceptibility index than another does. The hybrid AHP-FR model (Section 3.3.2) relaxes this assumption by multiplying each class FR value by the AHP-derived weight of its parent factor, thereby explicitly incorporating differences in factor importance.

3.3.2 Hybrid AHP-frequency ratio (AHP-FR) model

The hybrid AHP-FR model mathematically reconciles expert-derived AHP weights with data-driven FR weights through multiplicative adjustment (Chandra et al. 2026; Das et al. 2026). The landslide susceptibility index (LSI) is calculated as follows:

$$LSI = \Sigma (WAHP_j \times FR_{ij}) \quad (10)$$

where:

LSI = Landslide susceptibility index for each pixel

$WAHP_j$ = Normalized AHP weight for factor j (derived from pairwise comparison matrix)

FR_{ij}= Frequency ratio value for class i of factor j

The hybrid AHP-FR model captures interfactor importance through AHP weights while incorporating intrafactor class susceptibility through FR values.

3.3.3 Hybrid AHP-NFR model

The hybrid AHP-normalized frequency ratio (AHP-NFR) model represents a methodological refinement of the standard AHP-FR hybrid. While the AHP-FR model (Section 3.3.2) multiplies AHP factor weights by raw FR values, the resulting landslide susceptibility index (LSI) can exhibit substantial numerical range variation across factors because raw FR values are unbounded

(theoretically ranging from zero to infinity). In the study area, the raw FR values range from 0.000 (quaternary deposits, certain LULC classes) to 6.366 (slope >40°), indicating that extreme FR values from a single factor class can disproportionately dominate the summed LSI, potentially masking the contributions of other important factors.

The AHP-NFR model addresses this scaling imbalance through probability normalization. For each conditioning factor j with m classes, the normalized frequency ratio P_{ij} for class i is calculated as:

$$P_{ij} = \frac{FR_{ij}}{\sum_{i=1}^{m} FR_{ij}} \quad (11)$$

where FR_ij is the raw frequency ratio of class i, and the denominator is the sum of all FR values across the m classes of factor j (Table 7). This transformation constrains the normalized ratings within each factor to sum to unity ($\sum P_{ij} = 1.0$), thereby (i) equalizing the potential contribution range of every factor to the final LSI regardless of the magnitude of its raw FR values; (ii) preserving the relative empirical susceptibility ranking among classes within each factor; and (iii) creating direct methodological parallelism with the pure AHP model, where subclass priority vectors also sum to unity by construction.

The LSI for the AHP-NFR model is subsequently calculated as:

$$LSI = \sum_{j=1}^{n} (WAHP_j \times P_{ij}) \quad (12)$$

where $WAHP_j$ is the AHP-derived normalized weight for factor j (identical to the weights used in both the pure AHP and AHP-FR models) and where P_{ij} is the probability-normalized FR value for class i of factor j. This formulation enables a controlled examination of whether normalizing within-factor class ratings—effectively removing the influence of differing FR magnitude ranges across factors—improves or degrades predictive performance relative to the raw FR hybrid.

3.4 Generalization of the landslide susceptibility index (LSI) calculation

After determining the factor weights and class ratings, the LSI for each pixel was calculated via a weighted linear combination approach. For each of the three weighting schemes, the LSI was calculated separately to enable direct comparison:

$$LSI = \sum_{j=1}^{n} (Wmodel_j \times R_{ij}) \quad (13)$$

where $Wmodel_j$ is the factor weight derived from the respective model (AHP, AHP-FR, and AHP-NFR), and R_{ij} is the normalized class rating.

The LSI calculation was performed via the Raster Calculator tool in ArcGIS 10.7.1. To facilitate interpretation, the continuous LSI values were classified into five susceptibility zones (very low, low, moderate, high, very high) via the natural breaks (Jenks) optimization method.

4. Results

4.1 Thematic Maps of the Study Area

Thematic maps for all nine conditioning factors were generated via ArcGIS 10.7.1 and are presented in Figure 5. Each factor was rasterized at a 30 m resolution and classified into discrete categories on the basis of natural break optimization and domain knowledge, and classification schemes were established from comparable LSM studies. The spatial patterns of each factor and their relationships with the observed landslide distribution are described below.

4.1.1 Slope angle

The slope angle is a fundamental control on landslide susceptibility, as it directly governs the gravitational shear stress acting on slope materials (Abdo et al. 2022). On gentle slopes, a low flow velocity promotes water infiltration and progressive soil saturation, whereas steeper slopes generate rapid surface runoff and higher downslope driving forces, both of which increase the failure probability under different hydrological conditions (Choudhari et al. 2014; Ali et al. 2019). Slope angles were derived

from the ASTER DEM (30 m resolution) via the spatial analyst slope tool and classified into five intervals on the basis of natural breaks and observed landslide distribution patterns: 0–10°, 10–20°, 20–30°, 30–40°, and >40° (Figure 5a). The study area is dominated by gentle to moderate terrain, with the 0–10° class occupying the largest proportion of the area (58.98%, Table 9), which corresponds primarily to the southwestern alluvial plains and broad valley floors. Steep slopes (>30°) are concentrated along the Myoraksan and Songaksan mountain ranges. The 20–30° and 30–40° classes exhibit the highest landslide density in the study area, which is consistent with the threshold slope range for shallow translational failure initiation in weathered phyllitic and gneissic terrain.

4.1.2 Lithology

Lithology is a primary controlling factor in landslide susceptibility, governing the intrinsic strength, permeability, weathering characteristics, and cohesion of geological materials. Different lithological units exhibit distinct levels of inherent landslide vulnerability depending on their mineralogical composition, degree of fracturing, and weathering susceptibility (Das et al. 2022; Trisnawati and Hidayatillah 2022). The lithological map was digitized from 1:200,000 geological maps (Geological Survey of the DPRK) and classified into four major rock units: Quaternary deposits; sedimentary rocks (primarily the phyllite of the Saknyong Formation); metamorphic rocks (gneiss, schist, and amphibolite of the Jangpung and Rangrim Groups); and intrusive rocks (granite of the Ongjin and Danchon Complexes) (Figure 5b). Sedimentary and metamorphic rocks dominate the central and northeastern sectors, respectively, whereas intrusive rocks form extensive batholiths in the western and southeastern portions. Quaternary deposits are concentrated in the southwestern plains. Metamorphic and sedimentary rocks exhibit the highest landslide susceptibility due to intense weathering, well-developed fracture cleavage in phyllites, and the presence of weak schistosity planes that serve as preferential failure surfaces.

4.1.3 Land use and land cover (LULC)

Previous studies have demonstrated the considerable influence of LULC on landslide occurrence through its effects on surface runoff generation, infiltration capacity, root cohesion, and anthropogenic slope modification (Shu et al. 2019; Tyagi et al. 2023; Guo et al. 2023). Strong linkages exist among agricultural land use, altered drainage patterns, and slope instability (Pande et al. 2018; Srivastava et al. 2020; Masood et al. 2023; Moharir et al. 2023), as vegetation removal and terracing modify infiltration capacity and surface runoff routing, thereby altering pore pressure regimes in underlying slope materials. The LULC map was derived from Landsat 8 OLI imagery (2022, 30 m resolution) via supervised classification with the maximum likelihood algorithm and was validated through field verification at 45 ground control points. Six LULC classes were identified: water body, swamp and flood flat, settlement, grassland, forest, and agriculture (Figure 5c). Grassland dominated the study area (54.96% of the pixels, Table 9), followed by forest (35.14%), reflecting the mountainous character of the region. Forest areas exhibit the highest landslide frequency, likely because of their association with steep, undeveloped slopes rather than any inherent destabilizing effect of tree cover—forests in the study area occupy the most rugged terrain where other land uses are impractical.

4.1.4 Rainfall

Rainfall is one of the most important triggering factors for landslides in monsoon-affected regions. High-intensity or prolonged rainfall generates surface runoff, elevates the soil moisture content, and produces positive pore water pressure within slope materials. As the pore water pressure increases, the effective normal stress and mobilized shear resistance decrease along potential failure surfaces, leading to shear instability and slope failure (Alexander and Formichi 1993; Devkota et al. 2013). The mean annual precipitation data (2015–2024) from six meteorological stations (Kumchon, Jangpung, Yonan, Peachon, Kaepung, and Kaesong) were interpolated via inverse distance weighting (IDW) to create a continuous rainfall surface. Five precipitation zones were classified on the basis of natural breaks: 999.1–1,126 mm, 1,126–1,189 mm, 1,189–1,265 mm, 1,265–1,348 mm, and 1,348–1,437.4 mm (Figure 5d). The spatial distribution exhibited a pronounced northeast-to-southwest decreasing gradient, reflecting orographic enhancement along the northeastern mountain fronts. The zones with the highest precipitation (1,265–1,437.4 mm) present the greatest landslide concentration, reflecting the strong influence of rainfall-induced saturation on slope instability, particularly when high-intensity monsoon rainfall coincides with the period of maximum antecedent soil moisture.

4.1.5 Elevation

Elevation operates as a profound indirect control on landslide susceptibility by governing the environmental and anthropogenic preconditions for slope failure. It determines the spatial distribution of vegetation communities and root-strength regimes, modulates the intensity and patterns of human land modification (settlement, agriculture, infrastructure), and dictates topographically driven hydrological processes such as water convergence zones and soil saturation patterns (Zhou et al. 2021; Chang et al. 2023). The elevation data were derived from the ASTER DEM and ranged from 1 to 750 m above sea level. Five classes were defined via natural breaks: 1–53 m, 53–123 m, 123–229 m, 229–400 m, and 400–750 m (Figure 5e). Low-elevation zones (1–53 m) dominate the study area (51.52% of pixels, Table 7), corresponding to the extensive alluvial plains. The 123–229 m class has the highest landslide frequency, reflecting the concentration of steep, fault-proximal terrain developed on weathered sedimentary and metamorphic rocks at moderate elevations. The highest elevation class (400–750 m) contains no recorded landslides in the training dataset, likely due to its limited spatial extent (1.75% of the area) and the predominance of resistant intrusive rocks at higher elevations.

4.1.6 Distance from Faults

Proximity to geological faults is a critical factor for landslide susceptibility, as tectonic movements fracture and weaken rock masses in adjacent areas, creating zones of reduced mechanical strength, enhanced permeability, and accelerated weathering (Klai et al. 2020; Sura et al. 2020). Fault zones serve as preferential pathways for groundwater infiltration and chemical weathering, progressively reducing rock mass quality with increasing proximity to the fault trace. The fault map was digitized from 1:200,000 geological maps, and Euclidean distance analysis was performed to create a continuous distance surface. On the basis of the spatial distribution of landslides relative to mapped fault lines, distances were classified into five buffer categories: 0–1,000 m, 1,000–2,000 m, 2,000–3,000 m, 3,000–4,000 m, and >4,000 m (Figure 5f). The 0–1,000 m buffer zone has the highest landslide concentration (50% of training landslides, FR = 1.919; Table 9), with landslide density decreasing systematically with increasing distance from fault traces. This strong spatial decay pattern confirms the dominant role of fault-proximal weakening in controlling landslide distribution within the study area.

4.1.7 Slope Aspect

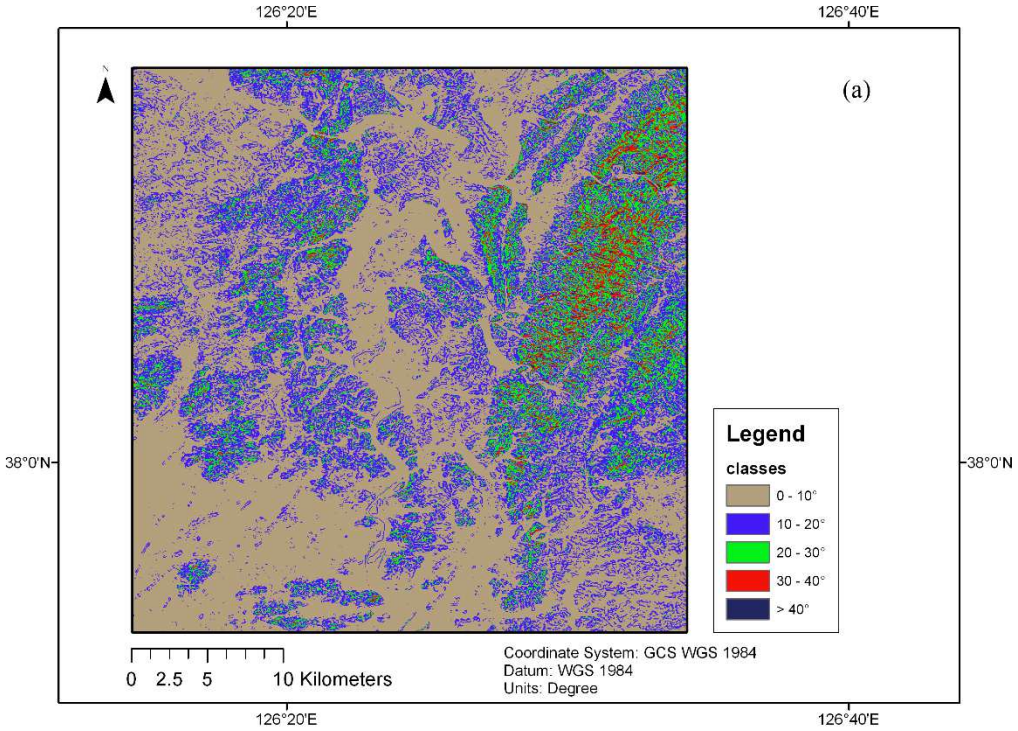
Slope aspect is a significant determinant of slope stability, particularly in the hilly terrain of the Northern Hemisphere, where aspect controls insolation receipt, evapotranspiration rates, freeze–thaw cycle frequency, and vegetation community composition (Meten et al. 2015). Compared with north-facing slopes, south-facing slopes receive greater direct solar radiation throughout the year, leading to greater diurnal temperature fluctuations, more frequent freeze–thaw cycling, and distinct vegetation and soil moisture regimes (Martha et al. 2013; Yalcin 2008). Consequently, weathering processes and human activities (agriculture, settlement) are often more pronounced on south- and southwest-facing slopes, contributing to increased landslide susceptibility (Egli et al. 2006). For this study, the slope aspect was derived from the ASTER DEM and categorized into nine directional classes: (1) flat (−1), (2) north (0–22.5° and 337.5–360°), (3) northeast (22.5–67.5°), (4) east (67.5–112.5°), (5) southeast (112.5–157.5°), (6) south (157.5–202.5°), (7) southwest (202.5–247.5°), (8) west (247.5–292.5°), and (9) northwest (292.5–337.5°) (Figure 5g). South-facing slopes (FR = 1.938) and southwest-facing slopes (FR = 1.468) exhibit the highest landslide frequencies, which is consistent with enhanced insolation-driven weathering and the predominance of monsoon rain-bearing winds from the south and southwest.

4.1.8 Curvature

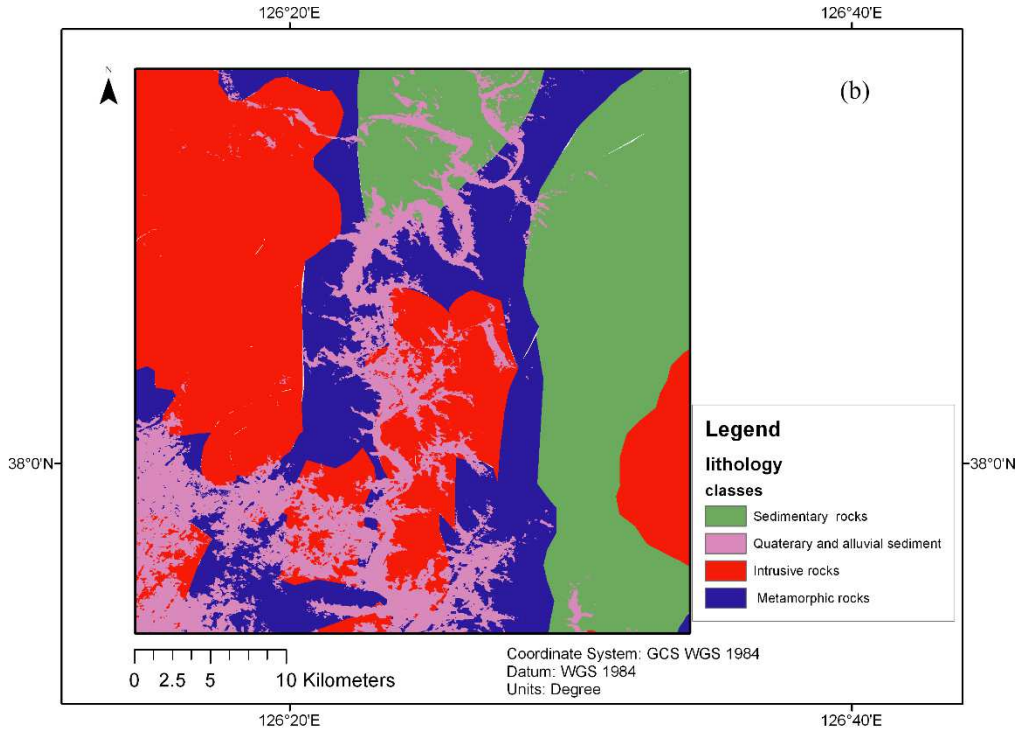
Curvature represents the shape of the slope profile and planform and is a key determinant of surface and subsurface water flow patterns on hillslopes. Profile curvature controls flow acceleration and deceleration, whereas plan curvature governs flow convergence and divergence (Wilson and Gallant 2000). A negative (concave) curvature indicates surface water convergence zones where subsurface flow accumulates, leading to higher soil moisture content, elevated pore water pressure, and increased susceptibility to both shallow translational sliding and rotational slumping. A positive (convex) curvature indicates surface water divergence zones where runoff disperses, leading to lower soil moisture and relatively reduced susceptibility (Rautela and Lakhera 2000). Greater absolute curvature values are typically associated with higher landslide probabilities due to concentrated flow erosion or tensile stress development at slope convexities. The curvature map was derived from the ASTER DEM via the spatial analyst curvature tool and classified into three classes: concave (negative values), flat (near-zero values), and convex (positive values) (Figure 5h). Concave slopes dominated the study area (47.06% of the pixels, Table 9) and presented the highest FR value (1.204), confirming their role in water concentration and progressive slope weakening. Convex slopes, while occupying a comparable proportion (44.08%), have lower landslide density (FR = 0.870), which is consistent with their divergent hydrologic behavior.

4.1.9 Distance from Rivers

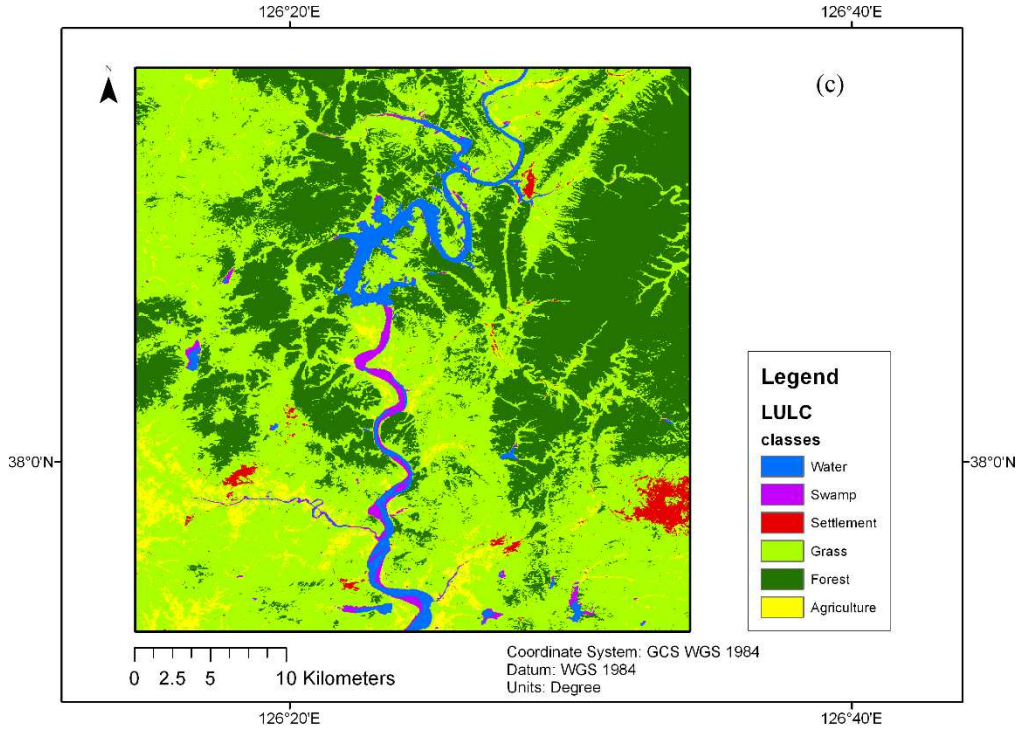
Slope stability is influenced by proximity to rivers through two primary mechanisms: lateral fluvial erosion at the slope toe, which steepens the slope profile and removes passive support, and elevated bank saturation during high-flow stages, which increases pore water pressure and reduces effective shear strength (Woldesenbet et al. 2023). Rivers and streams also control the base level of adjacent hillslopes, influencing long-term erosion rates and slope evolution. The river network was extracted from the ASTER DEM via hydrologic modeling tools (flow accumulation with a threshold of 500 contributing pixels) and validated against 1:50,000 topographic maps. Euclidean distance buffers were generated at four intervals: 0–500 m, 500–1,000 m, 1,000–1,500 m, and >1,500 m (Figure 5i). The FR analysis (Table 9) revealed no strong systematic distance-dependent pattern (FR range: 0.880–1.206), with all four distance classes showing FR values near unity. This suggests that, at the scale of this regional assessment, river proximity exerts a limited independent influence on landslide distribution, likely because the dominant controls—fault proximity, lithology, and slope angle—overwhelm the local effects of fluvial undercutting in controlling the spatial pattern of slope failure.



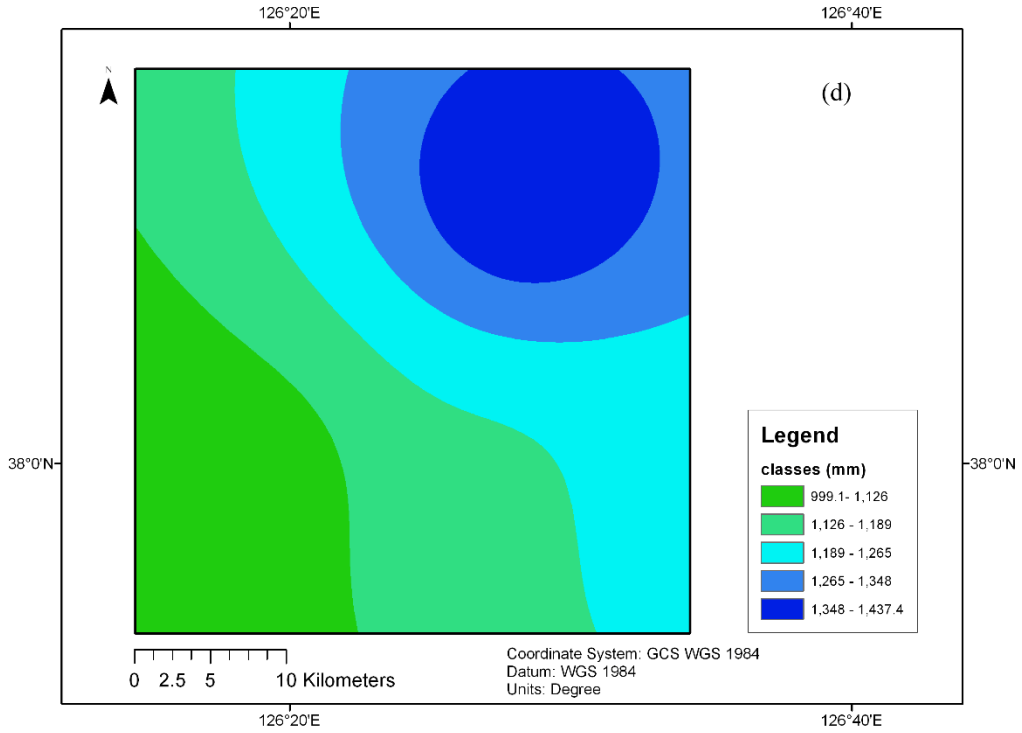
.


126°20'E
126°40'E
(b)
38°0'N
38°0'N
Legend
lithology
classes
Sedimentary rocks
Quaterary and alluvial sediment
Intrusive rocks
Metamorphic rocks
0 2.5 5 10 Kilometers
Coordinate System: GCS WGS 1984
Datum: WGS 1984
Units: Degree
126°20'E
126°40'E

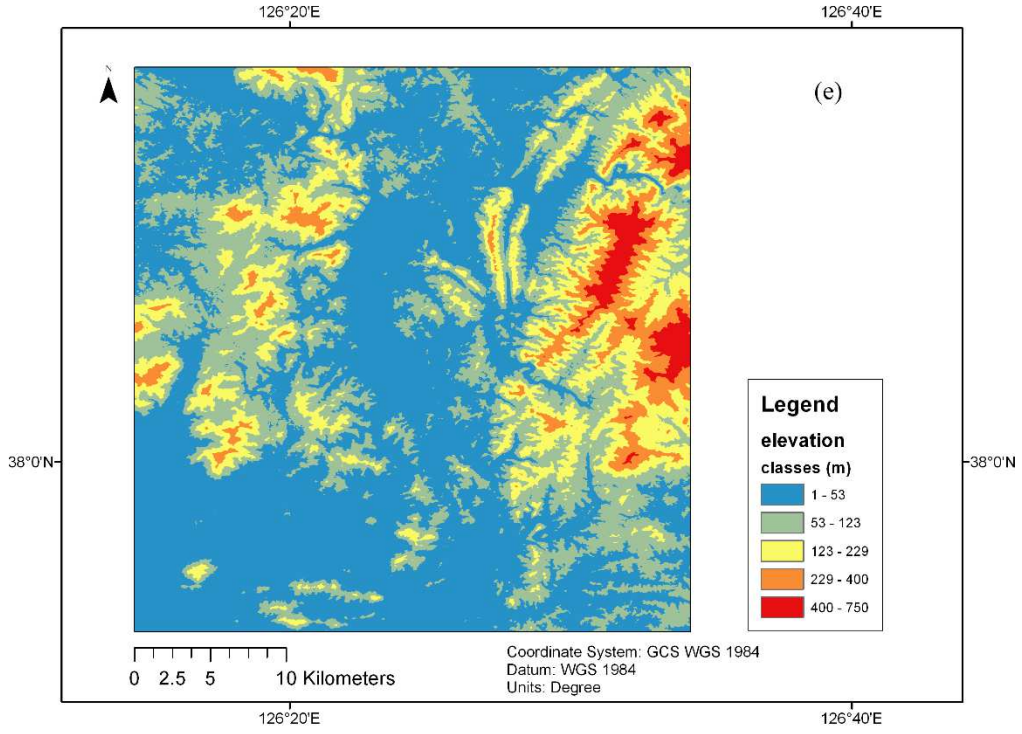
514


126°20'E
126°40'E
(c)
38°0'N
38°0'N
Legend
LULC
classes
Water
Swamp
Settlement
Grass
Forest
Agriculture
0 2.5 5 10 Kilometers
Coordinate System: GCS WGS 1984
Datum: WGS 1984
Units: Degree
126°20'E
126°40'E

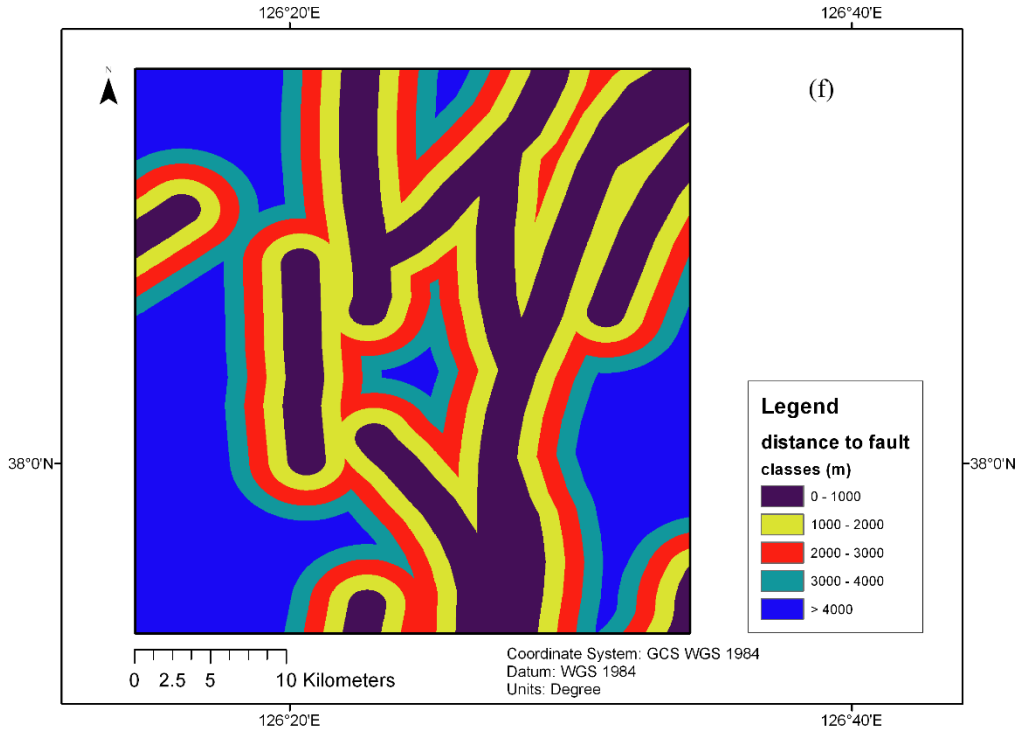
515


126°20'E
126°40'E
(d)
38°0'N
38°0'N
Legend
classes (mm)
999.1- 1,126
1,126 - 1,189
1,189 - 1,265
1,265 - 1,348
1,348 - 1,437.4
0 2.5 5 10 Kilometers
Coordinate System: GCS WGS 1984
Datum: WGS 1984
Units: Degree
126°20'E
126°40'E

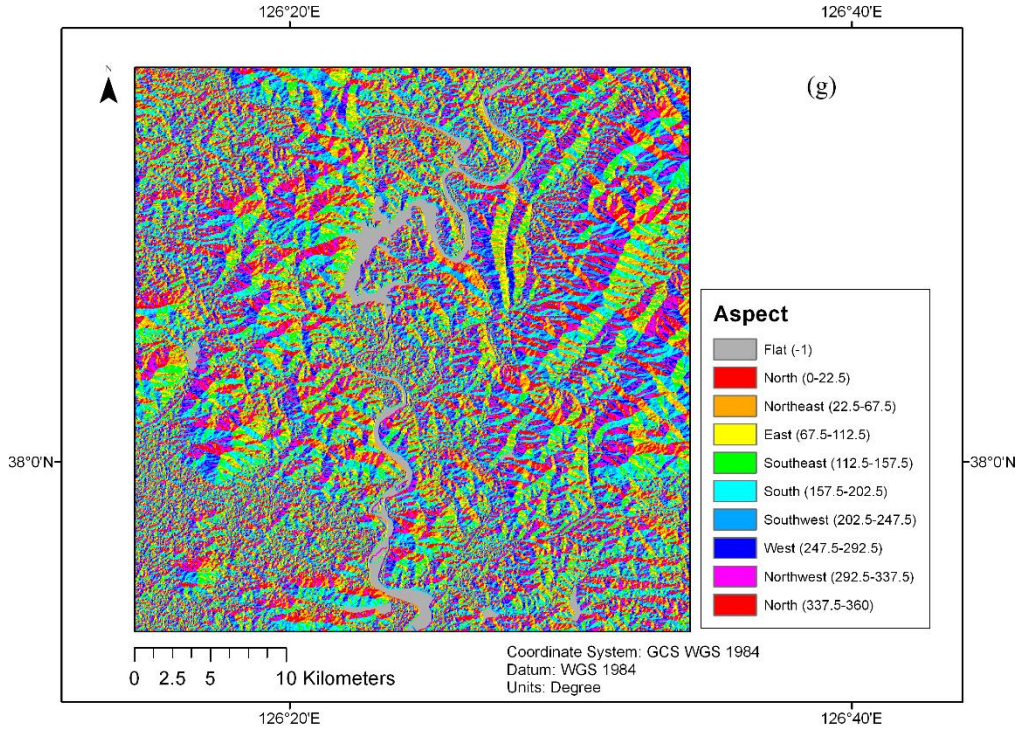
516


126°20'E
126°40'E
(e)
38°0'N
38°0'N
Legend
elevation
classes (m)
1 - 53
53 - 123
123 - 229
229 - 400
400 - 750
0 2.5 5 10 Kilometers
Coordinate System: GCS WGS 1984
Datum: WGS 1984
Units: Degree
126°20'E
126°40'E

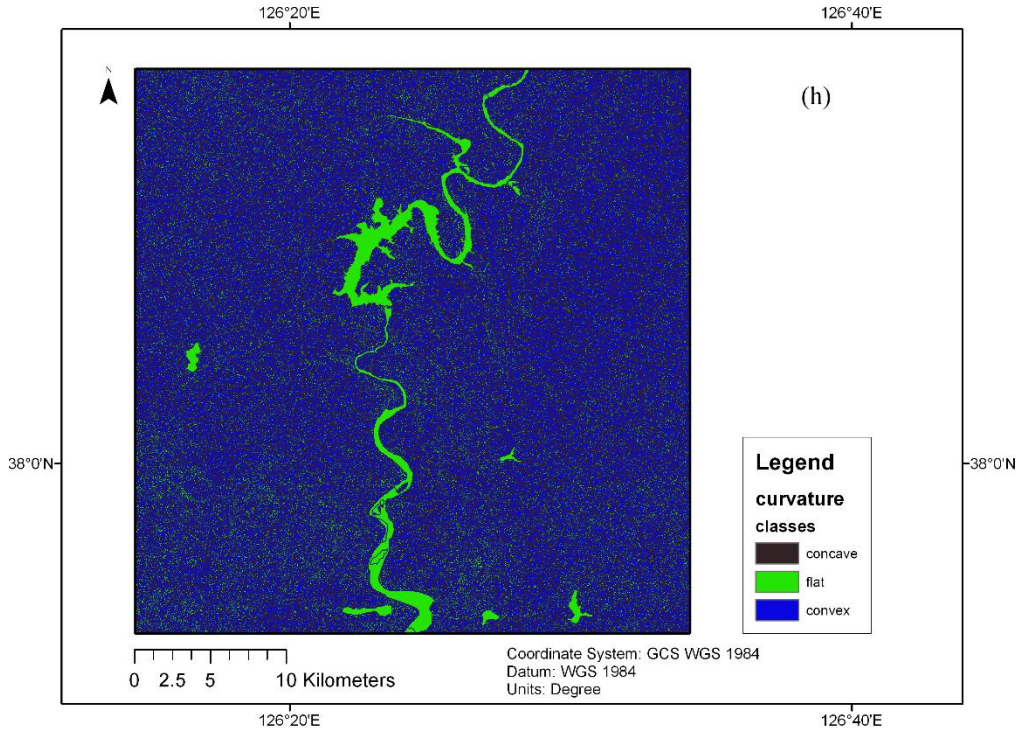
517


126°20'E
126°40'E
(f)
38°0'N
38°0'N
Legend
distance to fault
classes (m)
0 - 1000
1000 - 2000
2000 - 3000
3000 - 4000
> 4000
0 2.5 5 10 Kilometers
Coordinate System: GCS WGS 1984
Datum: WGS 1984
Units: Degree
126°20'E
126°40'E

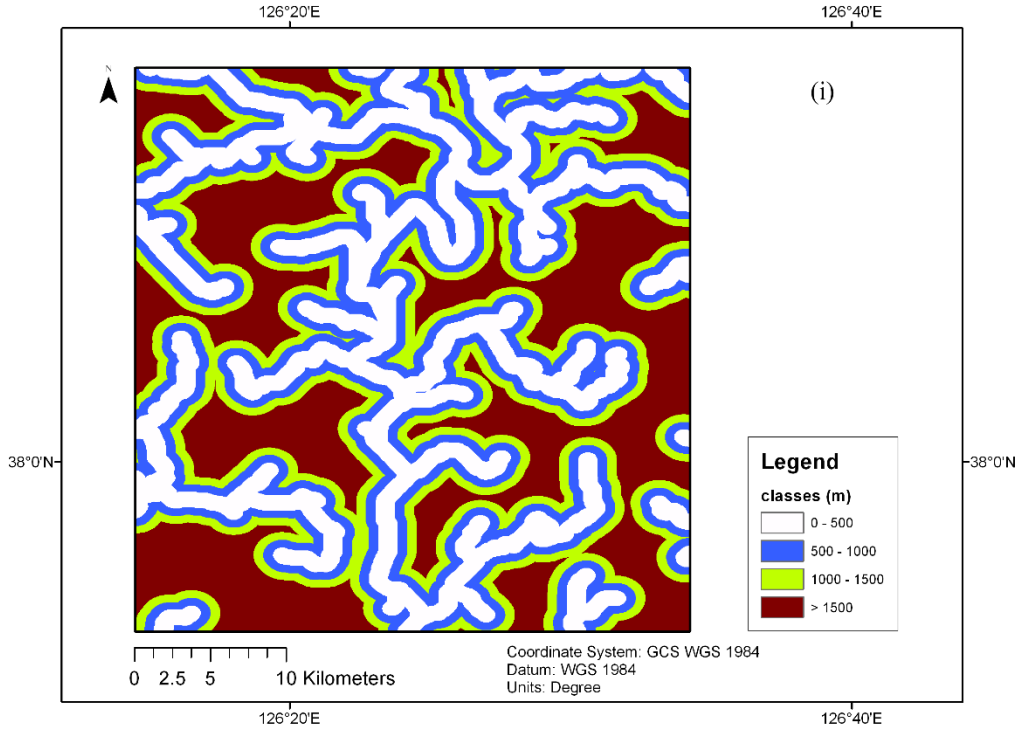
518


126°20'E
126°40'E
(g)
38°0'N
38°0'N
Aspect
Flat (-1)
North (0-22.5)
Northeast (22.5-67.5)
East (67.5-112.5)
Southeast (112.5-157.5)
South (157.5-202.5)
Southwest (202.5-247.5)
West (247.5-292.5)
Northwest (292.5-337.5)
North (337.5-360)
0 2.5 5 10 Kilometers
Coordinate System: GCS WGS 1984
Datum: WGS 1984
Units: Degree
126°20'E
126°40'E

519



520



521

522 **Figure 5** Thematic maps of the present study. a) slope, b) lithology, c) LULC, d) rainfall, e) elevation, f) distance to fault, g)
523 aspect, h) curvature, i) distance to river

524 4.2 AHP-Derived Factor Weights

The normalized AHP weights are presented in Table 5. Slope emerged as the most influential factor (27.82%), followed by lithology (18.88%), LULC (14.27%), and rainfall (10.85%). The consistency ratio (CR = 0.083) falls below the acceptable threshold of 0.10, confirming logical coherence.

Table 5 AHP pairwise comparison matrix and normalized weights

(Factors: F1=Slope, F2=Lithology, F3=LULC, F4=Rainfall, F5=Elevation, F6=Distance to Fault, F7=Aspect, F8=Curvature, F9=Distance to River)

Factor	F1	F2	F3	F4	F5	F6	F7	F8	F9	Weight	%
F1	1	2	2.5	3	3	4	5	5	6	0.2782	27.82
F2	0.5	1	1.5	2	2.5	3	4	4	5	0.1888	18.88
F3	0.4	0.67	1	1.5	2	2.5	3	3	4	0.1427	14.27
F4	0.33	0.5	0.67	1	1.5	2	2.5	2.5	3	0.1085	10.85
F5	0.33	0.4	0.5	0.67	1	2	2.5	2.5	3	0.0946	9.46
F6	0.25	0.33	0.4	0.5	0.5	1	1.5	1.5	2	0.0613	6.13
F7	0.2	0.25	0.33	0.4	0.4	0.67	1	1	1.5	0.0457	4.57
F8	0.2	0.25	0.33	0.4	0.4	0.67	1	1	1.5	0.0457	4.57
F9	0.17	0.2	0.25	0.33	0.33	0.5	0.67	0.67	1	0.0345	3.45

The pairwise matrix and the normalized weights of the classes of the main causative factors are shown in Table 6.

Table 6 Pairwise matrix and normalized weights of the classes of the main causative factors

Factor	class	[1]	[2]	[3]	[4]	[5]	[6]	[7]	[8]	[9]	Weight	CR
Slope	0 - 10°	1	0.33	0.17	0.14	0.25					0.048	
	10 - 20°	3	1	0.33	0.2	0.5					0.102	0.03
	20 - 30°	6	3	1	0.5	2					0.265	
	30 - 40°	7	5	2	1	3					0.435	
	> 40°	4	2	0.5	0.33	1					0.15	
Lithology	Sedimentary	1	2	3	7						0.49	
	Metamorphic	0.5	1	2	5						0.28	0.04
	Intrusive	0.33	0.5	1	4						0.16	
	Quaternary	0.14	0.2	0.25	1						0.07	
Aspect	Flat	1	0.2	0.25	0.2	0.33	0.14	0.17	0.25	0.25	0.022	
	N	5	1	2	1	3	0.33	0.5	2	2	0.124	0.05
	NE	4	0.5	1	0.5	2	0.25	0.33	1	1	0.07	
	E	5	1	2	1	3	0.33	0.5	2	2	0.124	
	SE	3	0.33	0.5	0.33	1	0.2	0.25	0.5	0.5	0.048	
	S	7	3	4	3	5	1	2	4	4	0.296	
	SW	6	2	3	2	4	0.5	1	3	3	0.178	
	W	4	0.5	1	0.5	2	0.25	0.33	1	1	0.07	
	NW	4	0.5	1	0.5	2	0.25	0.33	1	1	0.068	
Rainfall	999.1 - 1,126	1	0.67	0.5	0.4	0.33					0.101	0.01
	1,126 - 1,189	1.5	1	0.67	0.5	0.4					0.141	
	1,189 - 1,265	2	1.5	1	0.67	0.5					0.199	

Factor	class	[1]	[2]	[3]	[4]	[5]	[6]	[7]	[8]	[9]	Weight	CR
	1,265 - 1,348	2.5	2	1.5	1	0.67					0.267	
	1,348 - 1,437.4	3	2.5	2	1.5	1					0.292	
Distance to Fault	0-1000 m	1	3	5	7	8					0.505	0.02
	1000-2000 m	0.33	1	3	5	6					0.264	
	2000-3000 m	0.2	0.33	1	3	4					0.127	
	3000-4000 m	0.14	0.2	0.33	1	2					0.058	
	>4000 m	0.13	0.17	0.25	0.5	1					0.046	
LULC	Grass land	1	4	2	7	7	7				0.384	
	Agriculture	0.25	1	0.33	5	5	5				0.161	0.06
	Forest	0.5	3	1	6	6	6				0.302	
	Swamp & flood flat	0.14	0.2	0.17	1	1	1				0.051	
	Settlement	0.14	0.2	0.17	1	1	1				0.051	
	Water body	0.14	0.2	0.17	1	1	1				0.051	
elevation	1–53	1	0.1111	0.125	0.1667	0.5					0.0381	0.054
	53–123	9	1	1	2	4					0.3465	
	123–229	8	1	1	2	4					0.3384	
	229–400	6	0.5	0.5	1	3					0.199	
	400–750	2	0.25	0.25	0.3333	1					0.078	
Distance to River	0-500 m	1	2	3	4						0.467	0.01
	500-1,000 m	0.5	1	2	3						0.278	
	1,000-1,500 m	0.33	0.5	1	2						0.16	
	>1,500 m	0.25	0.33	0.5	1						0.095	
Curvature	Convex	1	2	7							0.591	0
	Concave	0.5	1	5							0.334	
	Flat	0.14	0.2	1							0.075	

4.3 Frequency ratio analysis

The frequency ratio values for all factor classes, which are calculated via the 60 training landslide points, are presented in Table 7. The FR analysis reveals several key patterns:

- Slope: Landslides are strongly concentrated in the 20–30° class (FR = 4.291). The highest FR occurs in the >40° class (FR = 6.366), although this class represents only 0.262% of the total pixel area.
- Lithology: Metamorphic rocks present the highest FR (1.899), followed by sedimentary rocks (FR = 1.482). Quaternary deposits exhibit null susceptibility (FR = 0.000).
- Aspect: South-facing slopes (FR = 1.938) and southwest-facing slopes (FR = 1.468) exhibit elevated landslide density.
- Rainfall: A positive gradient is evident, with the highest precipitation zone (1,348–1,437.4 mm) exhibiting FR = 1.715.
- Distance to Fault: Landslide density decreases systematically with distance from faults (0–1000 m: FR = 1.919; >4 000 m: FR = 0.264).
- LULC: Forest areas presented the highest FR (1.802).
- Elevation: The 123–229 m class presented the highest FR (2.884).
- Distance to River: No clear distance-dependent pattern emerges (FR = 0.880–1.206).
- Curvature: Concave slopes have the highest FR (1.204).

550 **Table 7** Frequency ratio (FR) for all factor classes

Factor	Classes	Pixel count	Pixel% (b)	Landslide Count	Landslide% (a)	FR(a/b)	Normalized FR (P_{ij})
Slope	0 - 10°	838678	58.980	10	16.667	0.2826	0.0201
	10 - 20°	399289	28.080	20	33.333	1.1871	0.0844
	20 - 30°	143598	10.099	26	43.333	4.2910	0.3051
	30 - 40°	36678	2.579	3	5.000	1.9384	0.1378
	> 40°	3723	0.262	1	1.667	6.3657	0.4526
Lithology	Sedimentary	384610	26.985	24	40.000	1.4823	0.3769
	Metamorphic	312670	21.937	25	41.667	1.8993	0.4829
	Intrusive	473937	33.252	11	18.333	0.5513	0.1402
	Quaternary	254062	17.825	0	0.000	0.0000	0.0000
Aspect	Flat	53144	3.725	0	0.000	0.0000	0.0000
	N	195432	13.698	7	11.667	0.8517	0.1046
	NE	171424	12.015	3	5.000	0.4161	0.0511
	E	135846	9.521	8	13.333	1.4004	0.1720
	SE	167400	11.733	6	10.000	0.8523	0.1047
	S	208644	14.624	17	28.333	1.9375	0.2380
	SW	178235	12.492	11	18.333	1.4676	0.1803
	W	142259	9.971	4	6.667	0.6686	0.0821
	NW	174356	12.221	4	6.667	0.5455	0.0670
Rainfall	999.1- 1,126	284411	19.951	11	18.333	0.9189	0.1649
	1,126 - 1,189	409577	28.731	7	11.667	0.4061	0.0729
	1,189 - 1,265	346313	24.293	17	28.333	1.1663	0.2093
	1,265 - 1,348	191268	13.417	11	18.333	1.3664	0.2452
	1,348 - 1,437.4	193986	13.608	14	23.333	1.7147	0.3077
Distance to Fault	0-1000 m	371803	26.060	30	50.000	1.9187	0.4110
	1000-2000 m	307167	21.529	16	26.667	1.2386	0.2654
	2000-3000 m	218940	15.345	5	8.333	0.5430	0.1163
	3000-4000 m	169127	11.854	5	8.333	0.7030	0.1506
	>4000 m	359703	25.212	4	6.667	0.2644	0.0567
LULC	Grass land	782855	54.962	21	35.000	0.6368	0.2268
	Agriculture	64387	4.520	1	1.667	0.3687	0.1313
	Forest	500504	35.139	38	63.333	1.8024	0.6419
	Swamp & flood flat	17298	1.214	0	0.000	0.0000	0.0000
	Settlement	16125	1.132	0	0.000	0.0000	0.0000
	Water body	43183	3.032	0	0.000	0.0000	0.0000
elevation	1~53	735110	51.524	3	5.000	0.0970	0.0154
	53~123	403105	28.254	29	48.333	1.7107	0.2715
	123~229	189630	13.291	23	38.333	2.8841	0.4577

	229~400	73893	5.179	5	8.333	1.6090	0.2554
	400~750	25002	1.752	0	0.000	0.0000	0.0000
Distance to River	0-500 m	378231	26.510	14	23.333	0.8802	0.2166
	500-1,000 m	328558	23.029	14	23.333	1.0132	0.2494
	1,000-1,500 m	276137	19.354	14	23.333	1.2056	0.2967
	>1,500 m	443814	31.107	18	30.000	0.9644	0.2373
Curvature	Concave	671377	47.057	34	56.667	1.2042	0.4565
	Flat	126531	8.869	3	5.000	0.5638	0.2137
	Convex	628832	44.075	23	38.333	0.8697	0.3297

4.4 Landslide susceptibility maps

The LSI values for the three weighting schemes were classified into five susceptibility zones via natural breaks (Figures 6–8, Table 8).

4.4.1 Pure AHP model

The pure AHP susceptibility map (Figure 6, Table 8) classifies 28.36% of the study area as high or very high susceptibility (20.82% high, 7.54% very high).

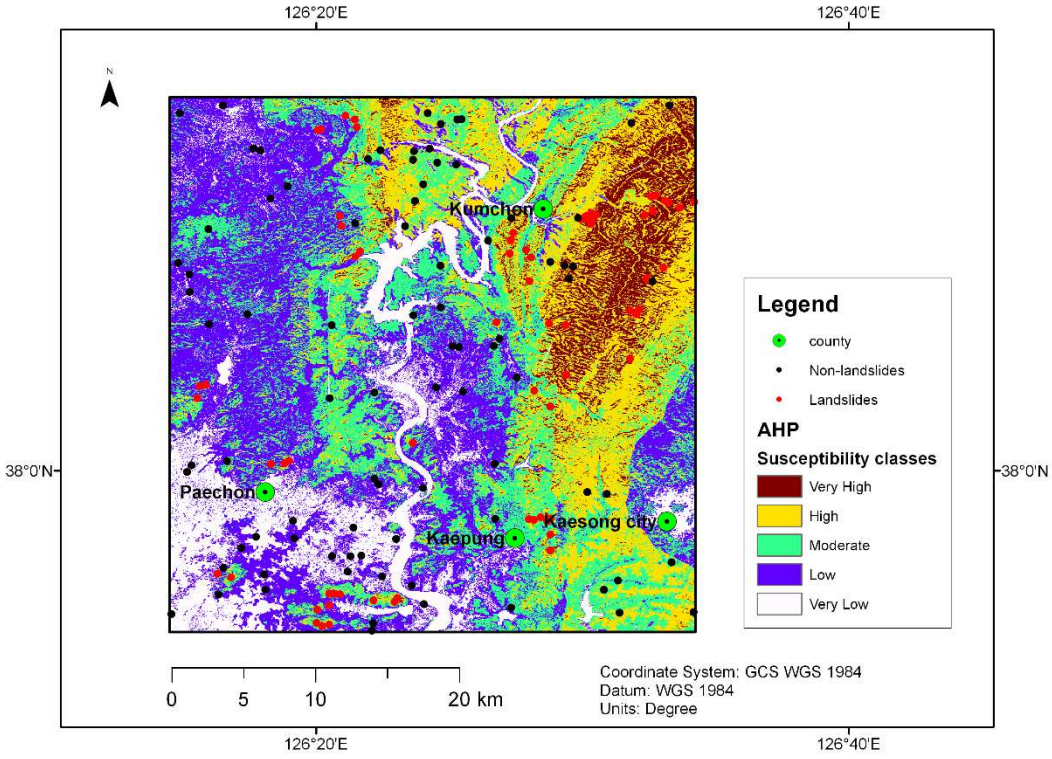


Figure 6 Landslide susceptibility map via the pure AHP model

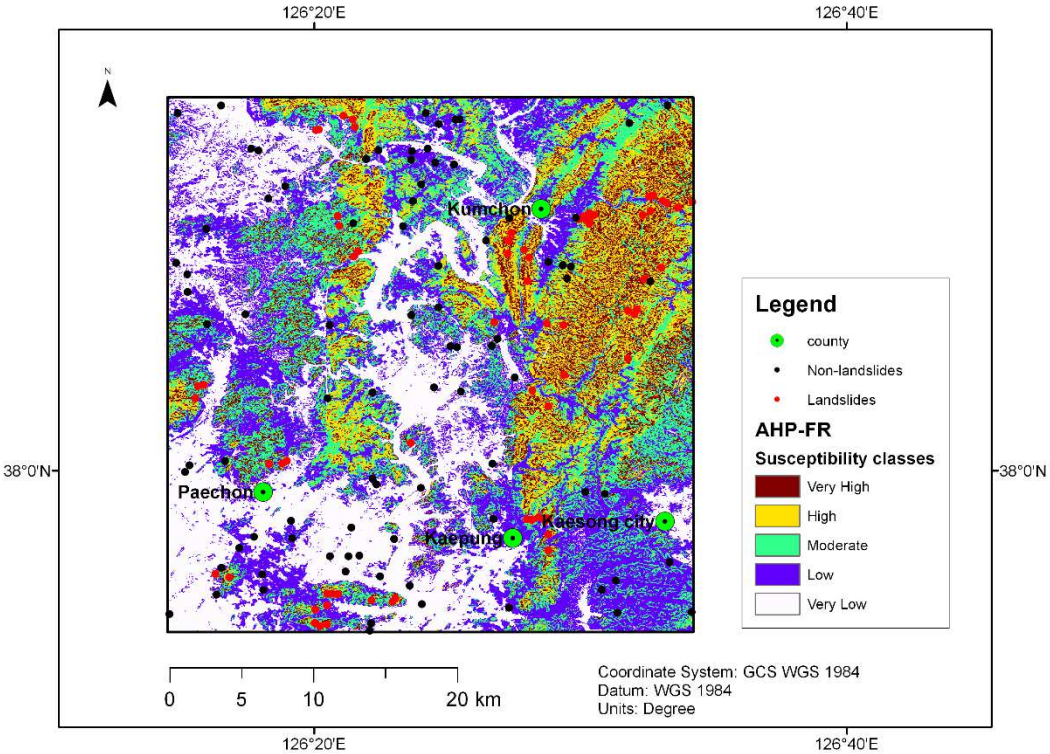
These elevated susceptibility zones are predominantly concentrated along the middle reaches of the Ryesong River and its tributary network, corresponding to steep slopes (20–40°) underlain by Paleozoic sedimentary rocks (primarily the phyllite of

the Saknyong Formation) on south- and southwest-facing aspects. The very low and low susceptibility categories collectively dominate 47.03% of the study area, occurring primarily in the southwestern alluvial plains (Quaternary deposits, slope <10°) and flat intermontane basins. The moderate category occupies 24.62% of the area, forming a transitional buffer between high-susceptibility mountainous terrain and low-susceptibility valley floors. The relatively large proportion of high and very high zones (28.36%) reflects the expert-weighted emphasis on slope and lithology as dominant factors, which tends to produce more extensive high-susceptibility designations than data-driven alternatives.

4.4.2 Hybrid AHP–FR model

The hybrid AHP-FR susceptibility map (Figure 7, Table 8) represents the spatial synthesis of expert-derived factor weights and empirically calibrated class ratings. This model produces the most conservative susceptibility zonation among all three models, with the smallest proportion of high-susceptibility areas (22.08% combined high and very high: 12.12% high, 9.96% very high) and the largest very low category (29.39%). This conservative behavior arises because the FR values effectively downweight classes that, despite expert perceptions of high susceptibility, contain relatively few training landslides. For example, while the Pure AHP model assigns high ratings to all steep slope classes, the FR analysis reveals that the 30–40° class (FR=1.938) has substantially lower landslide density than the 20–30° class (FR=4.291), leading to more selective high-susceptibility designation.

Spatially, the high and very high zones are concentrated in three distinct domains: (i) the northeastern mountainous sector, where steep metamorphic terrain coincides with the highest rainfall zone (1,348–1,437 mm) and where there is dense forest cover; (ii) the central Ryesong River corridor, characterized by fault-proximal (0–1000 m) sedimentary lithology on south-facing slopes; and (iii) isolated patches in the southwestern uplands corresponding to convex-to-concave transitional slopes in intrusive rock terrain. The very low susceptibility designation dominates the extensive Quaternary alluvial plains (26.06% of the study area is 0–1000 m from faults but with FR=0.000 for Quaternary deposits). The more selective spatial allocation of high susceptibility by AHP-FR—designating fewer areas as dangerous but correctly identifying landslide-prone zones with greater precision—is quantitatively validated by its superior capture efficiency (Section 4.5.4).



.

Figure 7 Landslide susceptibility map via the hybrid AHP-FR model

4.4.3 Hybrid AHP-NFR model

The hybrid AHP-NFR susceptibility map (Figure 8, Table 8) occupies an intermediate position between the pure AHP and AHP-FR models in terms of susceptibility zone allocation. The combined high and very high zones constitute 27.33% of the study area (18.77% high, 8.56% very high), which is closer to the pure AHP proportion (28.36%) than to the AHP-FR proportion (22.08%). This expansion of high-susceptibility zones relative to AHP-FR reflects the normalization process: by constraining each factor's class ratings to sum to unity, factors with inherently narrow FR ranges (e.g., distance to river, where all class FR values fall between 0.880 and 1.206) contribute proportionally equal rating magnitude to the LSI as factors with wide FR ranges (e.g., slope, where FR ranges from 0.283--6.366). Consequently, the AHP-NFR model partially restores the influence of factors that the raw FR model effectively downweighs because of the limited empirical contrast among their classes.

Spatially, the AHP-NFR susceptibility zonation exhibited greater continuity of moderate and high zones along valley margins than did the more fragmented AHP-FR pattern. The Very Low and Low categories collectively occupy 42.76% of the study area (22.21% and 20.55%, respectively), a substantially smaller proportion than the AHP-FR model (57.65%) but closer to the pure AHP distribution. This intermediate spatial behavior suggests that while normalization successfully addresses scaling disparities across factors, it may partially reintroduce expert bias by equalizing the contribution range of factors that empirically exhibit weak discriminatory power, thereby inflating susceptibility estimates in areas where multiple moderately rated classes coincide.

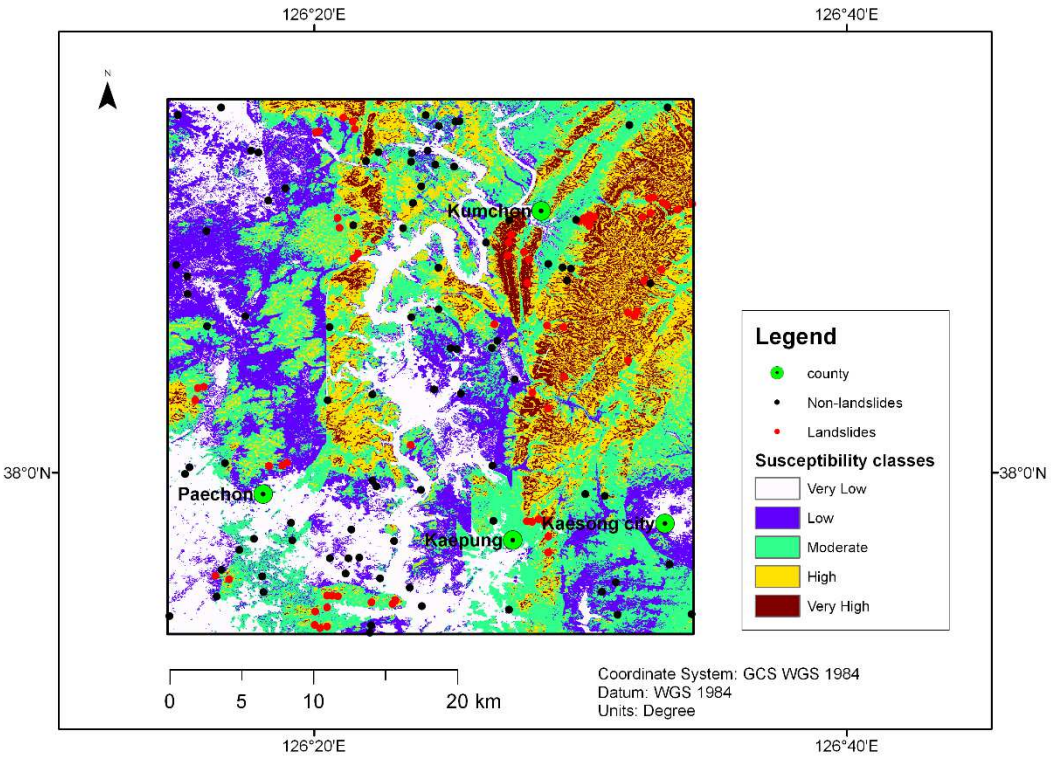


Figure 8 Landslide susceptibility map via the hybrid AHP-NFR model

Table 8 Area distributions of the susceptibility classes

Model	Very Low	Low	Moderate	High	Very High	High + Very High
Pure AHP	15.49%	31.54%	24.62%	20.82%	7.54%	28.36%
Hybrid AHP-FR	29.39%	28.26%	20.26%	12.12%	9.96%	22.08%
Hybrid AHP-NFR	22.21%	20.55%	29.90%	18.77%	8.56%	27.33%

4.5 Model validation

4.5.1 ROC curve analysis

ROC curve analysis (Figure 9, Table 9) demonstrated that all three models achieved acceptable to excellent predictive performance, with clear performance stratification consistent with the hybrid design hypothesis.

Table 9 Summary of the ROC-AUC validation results

Model	Training AUC	Validation AUC	AUC Difference	Performance Class
Pure AHP	0.8786	0.7988	0.0798	Fair
Hybrid AHP-FR	0.9592	0.9127	0.0464	Excellent
Hybrid AHP-NFR	0.9272	0.8624	0.0648	Good

The Hybrid AHP-FR model achieved the highest validation AUC (0.9127), followed by AHP-NFR (0.8624) and pure AHP (0.7988). Notably, the AHP-FR model exhibited the smallest difference between the training and validation AUCs (ΔAUC = 0.0464), suggesting superior generalization capacity and reduced overfitting compared with both pure AHP (ΔAUC = 0.0798) and AHP-NFR (ΔAUC = 0.0648). The relatively large performance gap between the training and validation datasets of the pure AHP model indicates that expert-driven class ratings, while internally consistent, do not generalize as effectively to independent landslide locations as empirically calibrated ratings do.

.

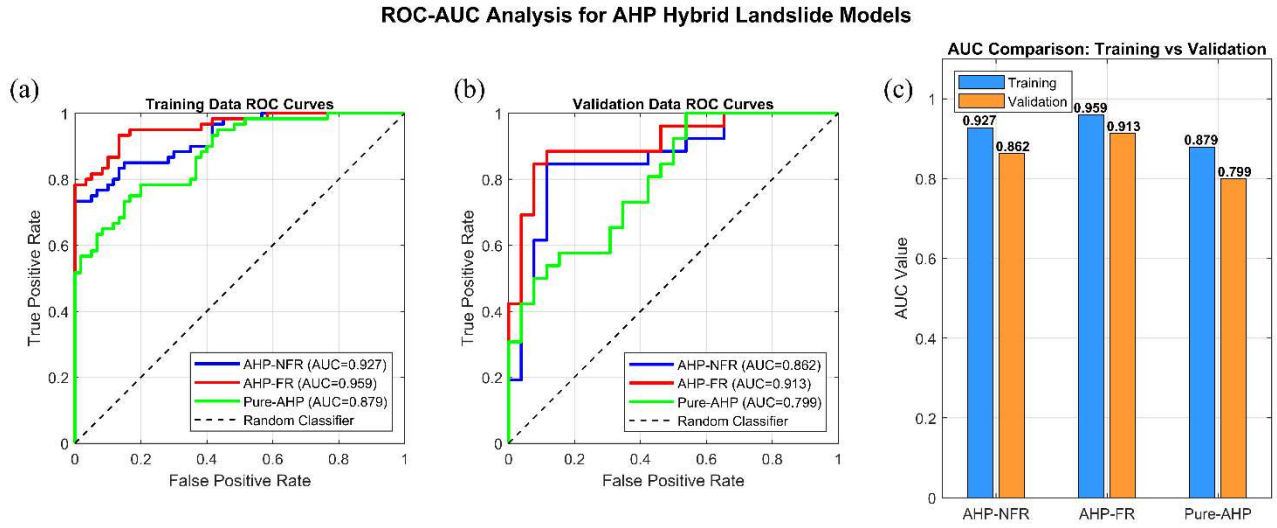


Figure 9 Model validation through receiver operating characteristic (ROC) curves of the (a) success rate, (b) prediction rate and (c) AUC comparison of the models

4.5.2 Bootstrap confidence intervals

Bootstrap resampling with 2000 iterations (Table 10, Figures 10, 11) confirmed the stability of the AUC estimates and enabled formal statistical comparisons among the models. The AHP-FR model achieved the highest bootstrap mean validation AUC (0.9126, 95% CI: 0.8199–0.9807), with the narrowest confidence interval width (0.1608), indicating high estimate precision. The AHP-NFR model achieved moderate performance (mean AUC 0.8622, 95% CI: 0.7511–0.9548, CI width = 0.2037), whereas the pure AHP model exhibited the lowest mean AUC (0.7971, 95% CI: 0.6654–0.9006) with the widest confidence interval (0.2352), confirming greater uncertainty in purely expert-driven predictions.

Table 10 Bootstrap confidence intervals for the prediction rate AUC (2000 iterations)

Model	Bootstrap Mean AUC	Original AUC	Bias	95% CI (Lower)	95% CI (Upper)	CI Width
Pure AHP	0.7971	0.7988	-0.0018	0.6654	0.9006	0.2352
Hybrid AHP-FR	0.9126	0.9127	-0.0001	0.8199	0.9807	0.1608
Hybrid AHP-NFR	0.8622	0.8624	-0.0002	0.7511	0.9548	0.2037

Table 11. Bootstrap pairwise comparison of validation AUCs

Model 1	Model 2	Mean ΔAUC	95% CI of Difference	p value	Significant (α=0.05)
AHP-FR	Pure AHP	+0.1156	[+0.0243, +0.2288]	0.0090	Yes
AHP-FR	AHP-NFR	+0.0504	[+0.0089, +0.1005]	0.0120	Yes
AHP-NFR	Pure AHP	+0.0652	[-0.0327, +0.1825]	0.2060	No

Pairwise bootstrap comparisons (Table 11, Figure 12) reveal that the AHP-FR model significantly outperforms both pure AHP ($p = 0.0090$) and AHP-NFR ($p = 0.0120$) at the $\alpha = 0.05$ significance level. The difference between AHP-NFR and pure AHP, while showing a positive mean difference of 0.0652 AUC units, does not reach statistical significance ($p = 0.2060$). These findings establish a clear performance hierarchy: AHP-FR > AHP-NFR ≈ pure AHP, with the AHP-FR hybrid achieving statistically significant superiority over both alternatives.

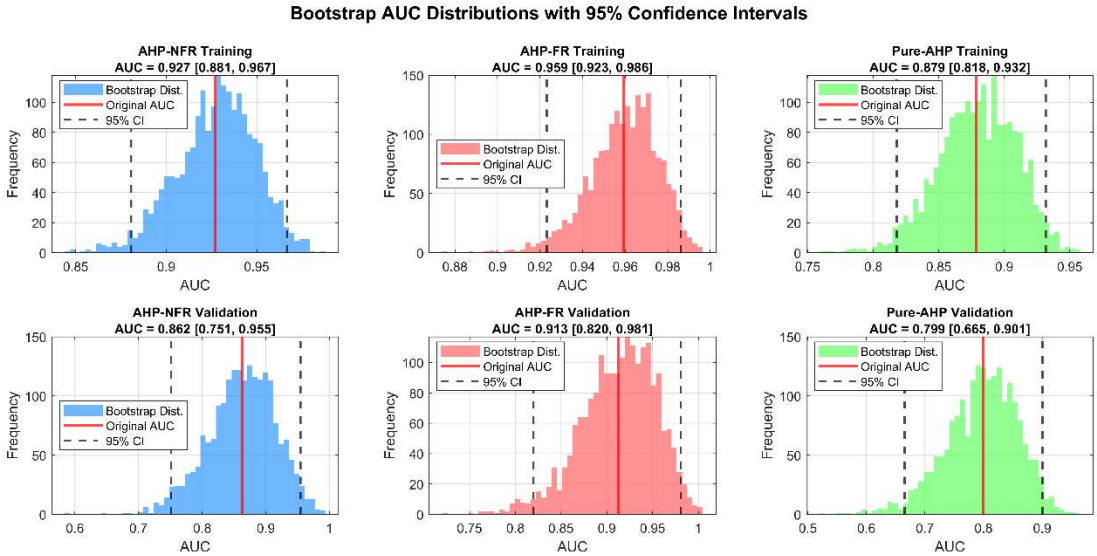
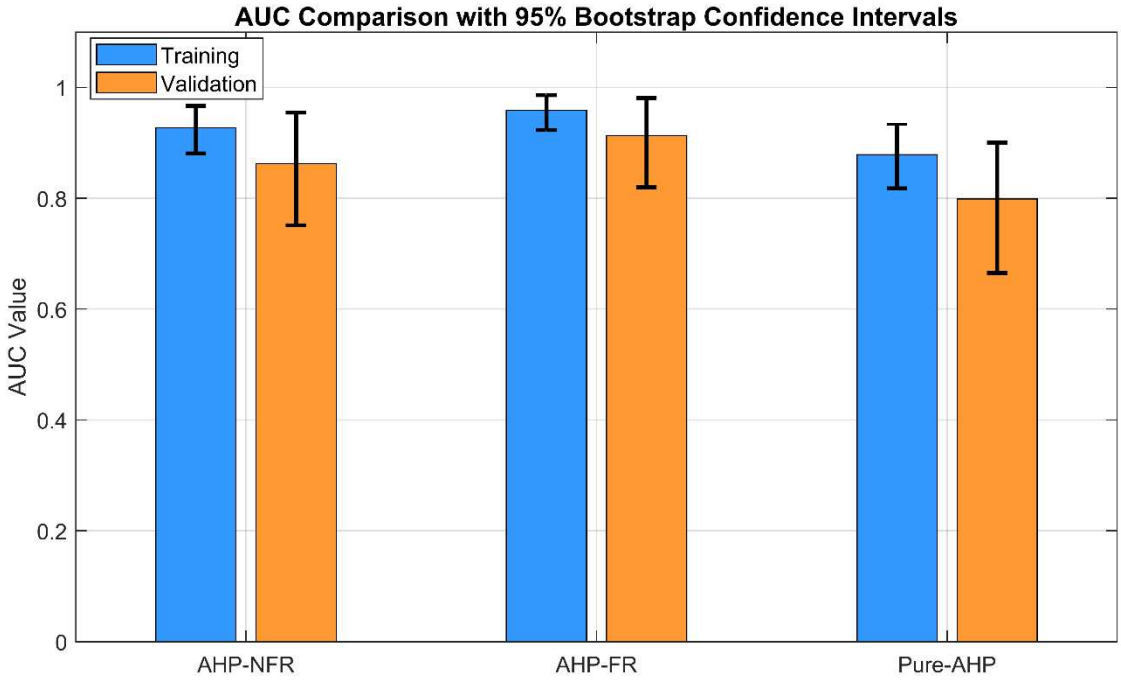
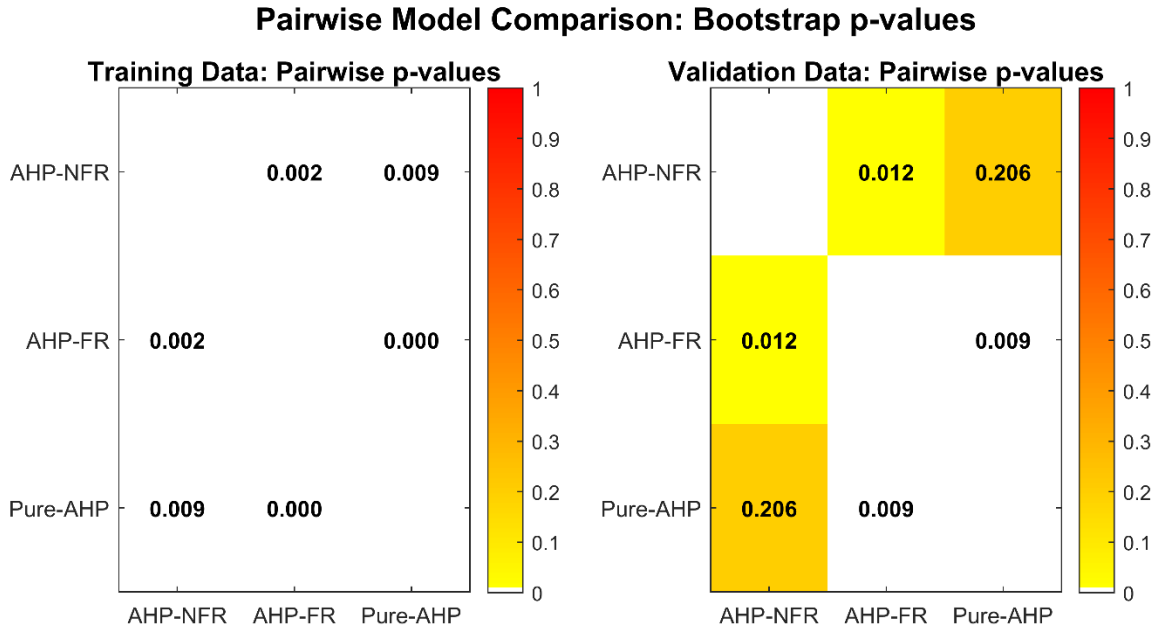


Figure 10 Bootstrap AUC distributions with 95% confidence intervals



637

638 **Figure 11** AUC comparison with 95% bootstrap confidence intervals



639

640 **Figure 12** Pairwise Model Comparison Bootstrap p values

641 4.5.3 Spatial cross-validation

Spatial cross-validation was implemented to assess model robustness under realistic spatial transferability conditions, where training and validation data are spatially segregated rather than randomly intermixed—a more stringent test than random cross-validation because it evaluates performance in geographically distinct terrains. Four cross-validation schemes were applied: standard fivefold random CV, spatial k-fold (k=5, blocks defined by spatial contiguity), spatial block CV (dividing the study area into regular grid blocks), and spatially clustered CV (grouping landslides by geomorphological subregions) (Figure 13).

Table 12 Spatial cross-validation results (mean AUC)

Model	Standard CV	Spatial K-Fold	Spatial Block	Spatial Clustered	Performance Degradation
Pure AHP	0.8528	0.8367	0.8557	0.7837	1.6%
Hybrid AHP-FR	0.9468	0.9331	0.9203	0.9075	1.4%
Hybrid AHP-NFR	0.9072	0.8806	0.8554	0.8405	2.7%

The AHP-FR model consistently achieved the highest mean AUC across all spatial cross-validation schemes (Table 12), with the smallest performance degradation when transitioning from standard to spatial k-fold validation (ΔAUC = -0.0136, 1.4% reduction). This minimal spatial sensitivity indicates that the AHP-FR model captures physically meaningful susceptibility relationships that generalize across the study area rather than fitting to localized, spatially autocorrelated patterns. The AHP-NFR model exhibited the greatest performance degradation (2.7%), suggesting that normalization may partially reintroduce spatial nonstationarity by equalizing factor contributions irrespective of the regional geomorphological context. The pure AHP model showed intermediate spatial stability (1.6% degradation) but from a substantially lower baseline performance level, confirming that expert-driven models, while spatially consistent, lack the empirical calibration necessary for high-accuracy spatial prediction.

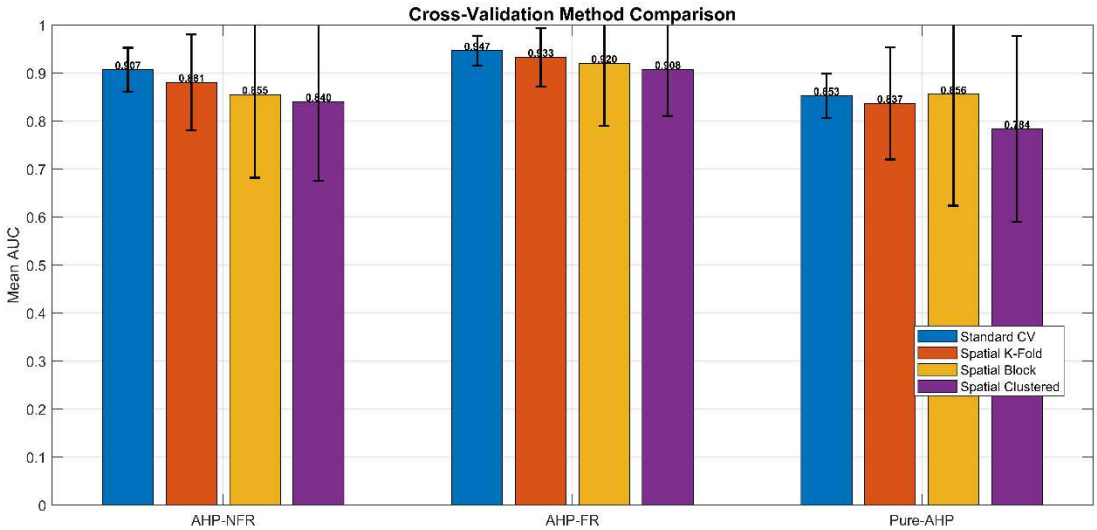


Figure 13 Comparison of four cross-validation schemes

4.5.4 Validation of Landslide Capture Efficiency

The practical utility of susceptibility maps for hazard mitigation and land-use planning depends not only on aggregate AUC metrics but also on the spatial concentration of validation landslides within the highest susceptibility zones. The capture

efficiency ratio (CER) quantifies this concentration by dividing the percentage of validation landslides captured in high and very high zones by the percentage of study area classified as high or very high:

$$CER = (\%\ captured)/(\%\ Area\ (High + Very\ High)) \qquad (14)$$

Table 13 Comparative validation of the landslide capture efficiency

Model	% Area (High + Very High)	Validation Landslides in H+VH (n)	% Captured	CER
Pure AHP	28.36	15	57.7	2.03
Hybrid AHP-FR	22.08	18	69.2	3.13
Hybrid AHP-NFR	27.33	17	65.4	2.39

The AHP-FR model achieves the highest CER (3.13), capturing 69.2% of the validation landslides within only 22.08% of the study area (Table 13). This represents a 54% improvement in capture efficiency over pure AHP (CER = 2.03) and a 31% improvement over AHP-NFR (CER = 2.39). The practical implications are substantial: for regional land-use planning applications where high-susceptibility zones are subject to development restrictions or enhanced monitoring requirements, the AHP-FR model minimizes the restricted area while maximizing the proportion of actual landslide locations within those restrictions. The AHP-NFR model's intermediate CER (2.39) reflects its normalized weighting scheme, which expands the high-susceptibility designation relative to AHP-FR but captures proportionally fewer landslides per unit area.

5. Discussion

This study employed a controlled three-model comparative framework to quantify the individual contribution of the class-rating methodology to landslide susceptibility model performance while holding factor-level weights constant through a single AHP hierarchy (CR=0.083). The results establish a clear and statistically significant performance hierarchy: AHP-FR (AUC=0.9127) > AHP-NFR (AUC=0.8624) > **pure** AHP (AUC=0.7988), with AHP-FR significantly outperforming both alternatives ($p<0.02$).

*Superiority of the AHP-FR **hybrid***

The superior performance of the AHP-FR model can be attributed to its dual optimization of the two distinct components of the susceptibility calculation. At the interfactor level, the AHP weights preserve the expert's structured understanding that certain conditioning factors fundamentally exert stronger geotechnical control on slope stability than others—an understanding that is consistently supported by physically based slope stability theory (Wilson and Gallant 2000). The dominance of slope (27.82%), lithology (18.88%), and LULC (14.27%) in the AHP hierarchy aligns with established geotechnical principles that slope angle governs gravitational driving forces, lithology controls material strength, and land cover modulates hydrological response (Alexander and Formichi 1993; Devkota et al. 2013).

At the intrafactor (class) level, FR values anchor susceptibility ratings in the empirical reality of the local landslide inventory, correcting expert perceptions that may not accurately reflect the observed spatial distribution of slope failures. Several instructive discrepancies between the AHP and FR class ratings illustrate this mechanism. The AHP subclass matrix assigned the highest susceptibility to the 30–40° slope class (weight=0.435), reflecting the expert's assumption that steeper slopes are consistently more hazardous. The FR analysis, however, revealed that the 20–30° class contains substantially higher landslide density (FR=4.291) than the 30–40° class does (FR=1.938), likely because the 20–30° range represents the threshold slope for widespread shallow failure initiation in the phyllitic soils of the study area, whereas slopes exceeding 40° occupy only 0.262% of the terrain and may be too steep to accumulate sufficient weathered material for landslide development. Similarly, the AHP

subclass matrix assigned moderate susceptibility to the 53–123 m elevation class (weight=0.347), whereas the FR analysis revealed that the 123–229 m class exhibited substantially higher landslide concentrations (FR=2.884), corresponding to the elevation band where fault-proximal, steep sedimentary terrain is most extensive.

By replacing subjective class ratings with FR values while retaining AHP factor weights, the hybrid model achieves a synergistic combination: the expert's macrolevel understanding of which factors matter most is preserved, whereas the inventory's microlevel information about which specific terrain conditions have historically failed is used to calibrate within-factor ratings. This explains why AHP-FR not only achieves higher overall accuracy but also produces more conservative (smaller high-susceptibility area, 22.08%) yet more precise (higher CER, 3.13) susceptibility zonation than the pure AHP does.

*Limited **benefit** of FR **normalization***

The AHP-NFR model was designed to address a potential limitation of raw FR values: their unbounded range (0.000--6.366 in this study) can theoretically allow extreme FR values from a single class to dominate the LSI calculation, potentially obscuring the contributions of other factors. The normalization procedure constrains within-factor class ratings to sum to unity, equalizing each factor's potential contribution range regardless of the empirical spread of its FR values.

However, the results demonstrate that this normalization does not improve the predictive performance—AHP-NFR (AUC=0.8624) performs significantly worse than AHP-FR ($p=0.012$). This finding suggests that the unequal contribution ranges of different factors, far from being a methodological flaw, actually encode meaningful information about the relative discriminatory power of each factor for landslide prediction. Factors with wide FR ranges (e.g., slope: 0.283–6.366) are precisely those with strong empirical associations with landslide occurrence, and allowing them to contribute proportionally more to the LSI improves predictive accuracy. Normalization, by artificially equalizing contribution ranges, effectively dilutes the influence of the most empirically informative factors while amplifying the contribution of factors with limited discriminatory power (e.g., distance to river: FR range 0.880–1.206). This explains the expanded high-susceptibility zones in the AHP-NFR model (27.33% vs. 22.08% for AHP-FR) and its lower CER (2.39 vs. 3.13).

From a methodological perspective, this result provides important caution: normalization of class ratings across factors, while mathematically elegant and conceptually parallel to AHP subclass priority vectors, can degrade performance when the empirical data contain genuine variation in factor discriminatory power. The raw FR values preserve this variation; normalization suppresses it.

Validation Framework Contributions

This study's validation framework extends beyond standard ROC-AUC reporting to incorporate three additional rigor-enhancing components recommended in recent methodological reviews (Reichenbach et al. 2018; Brenning 2005): bootstrap confidence intervals, spatial cross-validation, and capture efficiency analysis.

The bootstrap analysis with 2000 iterations enabled formal statistical inference on model differences, moving beyond the common practice of simply ranking models by AUC (Pham et al. 2019; Saha et al. 2024). The finding that AHP-FR significantly outperforms both alternatives ($p<0.02$) provides stronger evidence for model selection than AUC ranking alone. Furthermore, the substantially narrower confidence interval for AHP-FR (CI width=0.161) than for pure AHP (CI width=0.235) indicates that data-driven class ratings not only improve point estimate accuracy but also enhance prediction stability.

Spatial cross-validation revealed that AHP-FR results in the smallest performance degradation when it transitions from random to spatial resampling (1.4%), confirming that the model captures transferable physical relationships rather than fitting spatially autocorrelated noise (Brenning 2005). This is a critical property for landslide susceptibility models intended for application beyond their training domain. The greater degradation of AHP-NFR (2.7%) reinforces the interpretation that normalization reduces spatial generalizability by suppressing empirically meaningful variation in factor importance across the landscape.

The capture efficiency ratio provides a complementary perspective on model utility that is directly relevant to practitioners. For a given acceptable level of development restriction, decision-makers seek to maximize the proportion of actual landslides contained within restricted zones. The AHP-FR CER of 3.13—capturing 69.2% of landslides within 22.08% of the area—represents a substantial practical improvement over the pure AHP (CER=2.03, 57.7% within 28.36%), enabling more cost-effective hazard zoning.

Limitations and Future Research Directions

Several limitations should be acknowledged. First, the landslide inventory of 86 events, while adequate for the analytical methods employed, represents a moderate sample size. Larger inventories would enable more stable FR estimation, particularly for rare factor classes (e.g., slopes >40° with only 1 landslide pixel). Second, the factor-level AHP weights, while consistent across all three models, remain fundamentally expert dependent. Future work could explore data-driven factor weight derivation via machine learning feature importance metrics while maintaining the structured class-rating comparison framework developed here. Third, the AHP-NFR model implemented only one of several possible normalization strategies (probability normalization); alternative approaches such as min–max normalization or z score standardization may yield different results and warrant investigation. Fourth, while this study focused on static susceptibility factors, dynamic triggering factors—particularly antecedent rainfall conditions and seismic activity—influence the temporal probability of landslide occurrence and could be incorporated into future hybrid frameworks. Finally, although the spatial cross-validation results support model transferability within the study area, application to geomorphologically distinct regions would require independent validation.

6. Conclusion

This study presents a controlled comparative assessment of three landslide susceptibility mapping models—Pure AHP, Hybrid AHP-FR, and Hybrid AHP-NFR—applied to a 1,071 km² Ryesong River basin in the southwestern part of the Democratic People's Republic of Korea. By holding factor-level AHP weights constant (CR=0.083) while systematically varying the class-rating methodology, the experimental design isolates the specific contribution of empirical calibration to model performance. The principal findings are as follows:

1. The hybrid AHP-FR model achieves superior predictive performance (validated AUC=0.9127, excellent classification), significantly outperforming both the pure AHP (AUC=0.7988, p=0.009) and AHP-NFR (AUC=0.8624, p=0.012) models. This validates the hypothesis that expert-derived factor weights combined with data-driven class ratings produce optimal results.
2. Frequency ratio normalization does not improve performance. The AHP-NFR model (probability-normalized FR class ratings) underperformed AHP-FR despite addressing the theoretical concern of unequal factor contribution ranges. This finding indicates that variation in FR ranges across factors encodes meaningful information about differential factor discriminatory power that should be preserved rather than suppressed.
3. The AHP-FR model demonstrates superior spatial generalizability and practical utility. This method results in the smallest performance degradation under spatial cross-validation (1.4%), the narrowest bootstrap confidence intervals (CI width=0.161), and the highest capture efficiency (CER=3.13), concentrating 69.2% of the validation landslides within only 22.08% of the study area.
4. Expert knowledge alone is insufficient for accurate class-level susceptibility ratings. The pure AHP model, while internally consistent and producing interpretable susceptibility zonation, achieves only fair predictive performance and designates unnecessarily large areas as having high susceptibility, limiting its practical efficiency for land-use planning.

These findings have direct implications for landslide susceptibility mapping practices. The AHP-FR hybrid framework—which is computationally accessible, does not require specialized statistical software, and maintains transparency in both its expert-driven structure and its empirical calibration—should be adopted as the standard approach when both domain expertise and a moderate landslide inventory are available. The normalization of FR values, while theoretically appealing, is not recommended, as it demonstrably degrades performance. Future research should extend this controlled comparison framework to incorporate machine learning-derived factor weights and dynamic triggering factors while maintaining the methodological rigor of bootstrap uncertainty quantification and spatial cross-validation demonstrated here.

References

Abdelkader, M.M., Csámer, Á. (2025) Comparative assessment of machine learning models for landslide susceptibility mapping: a focus on validation and accuracy. *Nat Hazards* 121, 10299–10321. https://doi.org/10.1007/s11069-025-07197-0

Abdo, H.G. (2022) Assessment of landslide susceptibility zonation using frequency ratio and statistical index: a case study of Al-fawar basin, Tartous, Syria. *Int J Environ Sci Technol* 19, 2599–2618. https://doi.org/10.1007/s13762-021-03322-1

Achu, A., Thomas, J., Aju, C., Remani, P., Gopinath, G. (2022) Performance evaluation of machine learning and statistical techniques for modelling landslide susceptibility with limited field data. *Earth Sci Inform* https://doi.org/10.1007/s12145-022-00910-8

Alam, M., Siddiqui, A.N., Shamim, S.K. et al. (2025) A comparative evaluation of geostatistical techniques of frequency ratio (FR), Shannon Entropy (SE), and analytical hierarchy (AHP) in landslide prediction: a case study of Uttarakhand, India. *Discov Geosci* 3, 28. https://doi.org/10.1007/s44288-025-00138-1

Alexander, D., Formichi, R. (1993) *Landslide hazard and risk*. John Wiley & Sons, New York.

Arabameri, A., Saha, S., Chen, W., Roy, J., Pradhan, B., Bui, D.T. (2020) Flash flood susceptibility modelling using functional tree and hybrid ensemble techniques. *J Hydrol* 587, 125007. https://doi.org/10.1016/j.jhydrol.2020.125007

Bednarik, M., Yilmaz, I., Marschalko, M. (2012) Landslide hazard and risk assessment: a case study from the Hlohovec–Sereď landslide area in south-west Slovakia. *Nat Hazards* 64, 547–575. https://doi.org/10.1007/s11069-012-0257-7

Brenning, A. (2005) Spatial prediction models for landslide hazards: review, comparison and evaluation. *Nat Hazards Earth Syst Sci* 5, 853–862. https://doi.org/10.5194/nhess-5-853-2005

Chaiyaphan, C., Ransikarbum, K. (2020) Criteria analysis of food safety using the Analytic Hierarchy Process (AHP)—a case study of Thailand's fresh markets. *E3S Web Conf* 141, 02001. https://doi.org/10.1051/e3sconf/202014102001

Chandra, D., Debnath, S., Ghosh, D. et al. (2026) Flood hazard assessment using AHP–FR–Fuzzy ensemble of a sub-Himalayan catchment in a transboundary piedmont landscape of the Eastern Himalayas. *Nat Hazards* 122, 340. https://doi.org/10.1007/s11069-025-07766-3

Chatterjee, S., Simonoff, J.S. (2013) *Handbook of Regression Analysis*. John Wiley & Sons, New York.

Choudhari, K., Panigrahi, B., Paul, J.C. (2014) Morphometric analysis of Kharlikani watershed in Odisha, India using spatial information technology. *Int J Geomat Geosci* 4(4), 661–675.

Corominas, J., van Westen, C., Frattini, P. et al. (2014) Recommendations for the quantitative analysis of landslide risk. *Bull Eng Geol Environ* 73, 209–263. https://doi.org/10.1007/s10064-013-0538-8

Das, M., Gautam, G.K., Jain, S., Bhat, M.F., Mankar, A.K., Koner, R. (2026) A comparative analysis of AHP, FR, AHP-FR and LR models for landslide susceptibility mapping in Sikkim Himalaya, India. *Earth Surf Process Landforms* 51(2), e70257. https://doi.org/10.1002/esp.70257

Devkota, K.C., Regmi, A.D., Pourghasemi, H.R., Yoshida, K., Pradhan, B., Ryu, I.C. et al. (2013) Landslide susceptibility mapping using certainty factor, index of entropy and logistic regression models in GIS and their comparison at Mugling-Narayanghat road section in Nepal Himalaya. *Nat Hazards* 65, 135–165. https://doi.org/10.1007/s11069-012-0347-6

Dias, A.A.V., Gunathilake, A.A.J. (2025) Analytical Hierarchical Process (AHP) prioritization of landslide-causing factors. In: Abolmasov, B. et al. (eds) *Progress in Landslide Research and Technology, Volume 3 Issue 2, 2024*. Springer, Cham. https://doi.org/10.1007/978-3-031-72736-8_3

Feizizadeh, B., Blaschke, T. (2013) Examining urban heat island relations to land use and air pollution: multiple endmember spectral mixture analysis for thermal remote sensing. *IEEE J Sel Top Appl Earth Obs Remote Sens* 6, 1749–1756. https://doi.org/10.1109/JSTARS.2013.2263425

Golder, J., Bhandari, G. (2026) A comparative study among ensemble and independent statistical models: a high-accuracy and conservative framework for landslide susceptibility mapping in east Sikkim Himalaya. *Environ Earth Sci* 85, 92. https://doi.org/10.1007/s12665-025-12809-w

Guzzetti, F., Carrara, A., Cardinali, M., Reichenbach, P. (1999) Landslide hazard evaluation: a review of current techniques and their application in a multi-scale study, Central Italy. *Geomorphology* 31, 181–216. https://doi.org/10.1016/S0169-555X(99)00078-1

Hoa, P.V., Tuan, N.Q., Hong, P.V., Thao, G.T.P., Binh, N.A. (2023) GIS-based modeling of landslide susceptibility zonation by integrating the frequency ratio and objective–subjective weighting approach: a case study in a tropical monsoon climate region. *Front Environ Sci* 11, 1175567. https://doi.org/10.3389/fenvs.2023.1175567

Hosmer, D.W., Lemeshow, S. (2000) *Applied Logistic Regression*. John Wiley & Sons, New York.

Islam, M.R., Hosen, M.B., Hossain, M.M.M. et al. (2025) Future projections of landslide susceptibility in the Hill Tracts of Bangladesh: an AHP-based approach. *Earth Syst Environ* 9, 3017–3041. https://doi.org/10.1007/s41748-025-00776-y

Kim, H.U., Jong, S.I., Om, K.C. et al. (2025) Spatiotemporal variability of drought during 1951–2022 in the Democratic People's Republic of Korea and related atmospheric circulation patterns. *J Earth Syst Sci* 134, 63. https://doi.org/10.1007/s12040-024-02475-0

Ksantini, F., Sdiri, A., Aydi, A., Almeida-Ñauñay, A.F., Achour, H., Tarquis, A.M. (2025) A comparative study based on AHP and fuzzy logic approaches for landslide susceptibility zoning using a GIS-based multi-criteria decision analysis. *Euro-Mediterr J Environ Integr* 10, 649–668. https://doi.org/10.1007/s41207-024-00552-w

Kucuker, D.M. (2025) Analyzing landslide susceptibility of forest roads by analytical hierarchy process (AHP) in forest planning unit of Turkey. *Nat Hazards* 121, 2323–2345. https://doi.org/10.1007/s11069-024-06882-w

Liu, X., Shao, S., Shao, S. (2024) Landslide susceptibility zonation using the analytical hierarchy process (AHP) in the Great Xi'an Region, China. *Sci Rep* 14, 2941. https://doi.org/10.1038/s41598-024-53630-y

Melese, T., Belay, T., Andemo, A. (2022) Application of analytical hierarchal process, frequency ratio, and Shannon entropy approaches for landslide susceptibility mapping using geospatial technology: the case of Dejen district, Ethiopia. *Arab J Geosci* 15, 424. https://doi.org/10.1007/s12517-022-09672-5

Nath, N.K., Gautam, V.K., Pande, C.B., Mishra, L.R., Raju, J.T., Moharir, K.N., Rane, N.L. (2024) Development of landslide susceptibility maps of Tripura, India using GIS and analytical hierarchy process (AHP). *Environ Sci Pollut Res* 31, 7481–7497. https://doi.org/10.1007/s11356-023-31486-5

Ozdemir, A., Altural, T. (2013) A comparative study of frequency ratio, weights of evidence and logistic regression methods for landslide susceptibility mapping: Sultan Mountains, SW Turkey. *J Asian Earth Sci* 64, 180–197. https://doi.org/10.1016/j.jseaes.2012.12.014

Paek, R., Kang, H., Jon, G., Kim, Y., Kim, Y. (1993) *Geology of Korea*. Foreign Languages Books Publishing House, Pyongyang.

Panchal, S., Shrivastava, A.K. (2021) A comparative study of frequency ratio, Shannon's entropy and analytic hierarchy process (AHP) models for landslide susceptibility assessment. *ISPRS Int J Geo-Inf* 10(9), 603. https://doi.org/10.3390/ijgi10090603

Pham, B.T., Jaafari, A., Prakash, I., Bui, D.T. (2019) A novel hybrid intelligent model of support vector machines and the MultiBoost ensemble for landslide susceptibility modeling. *Bull Eng Geol Environ* 78(4), 2865–2886. https://doi.org/10.1007/s10064-018-1281-y

Pourghasemi, H., Gokceoglu, C., Pradhan, B., Moezzi, K. (2012) Landslide susceptibility mapping using a spatial multi criteria evaluation model at Haraz Watershed, Iran. In: *Terrigenous Mass Movements*, pp 23–49. Springer, Berlin. https://doi.org/10.1007/978-3-642-25495-6_2

Rebouh, N., Belkendil, A., Tout, F. et al. (2026) Landslide susceptibility assessment using hybrid geospatial, frequency ratio, and AHP models in Souk Ahras province, northeastern Algeria. *Sci Rep* 16, 2288. https://doi.org/10.1038/s41598-025-32062-2

Regmi, A.D., Yoshida, K., Pourghasemi, H.R., DhitaL, M.R., Pradhan, B. (2014) Landslide susceptibility mapping along Bhalubang-Shiwapur area of mid-western Nepal using frequency ratio and conditional probability models. *J Mt Sci* 11, 1266–1285. https://doi.org/10.1007/s11629-013-2847-6

Reichenbach, P., Rossi, M., Malamud, B.D., Mihir, M., Guzzetti, F. (2018) A review of statistically-based landslide susceptibility models. *Earth-Sci Rev* 180, 60–91. https://doi.org/10.1016/j.earscirev.2018.03.001

Roccati, A., Paliaga, G., Luino, F. et al. (2021) GIS-based landslide susceptibility mapping for land use planning and risk assessment. *Land* 10(2), 162. https://doi.org/10.3390/land10020162

Roy, J., Saha, S. (2019) Landslide susceptibility mapping using knowledge driven statistical models in Darjeeling District, West Bengal, India. *Geoenviron Disasters* 6(1), 1–18. https://doi.org/10.1186/s40677-019-0126-8

Saaty, T.L. (1977) A scaling method for priorities in hierarchical structures. *J Math Psychol* 15(3), 234–281.

Saaty, T.L. (1980) *The Analytic Hierarchy Process*. McGraw Hill, New York.

Saaty, T.L. (1990) How to make a decision: the analytic hierarchy process. *Eur J Oper Res* 48(1), 9–26. https://doi.org/10.1016/0377-2217(90)90057-I

Saaty, T.L. (2006) *Fundamentals of decision making and priority theory with the analytic hierarchy process*. RWS Publications, Pittsburgh.

Saaty, T.L., Vargas, L.G. (2001) *Models, methods, concepts & applications of the analytic hierarchy process*. Kluwer Academic, Boston.

Sachinthaka, R., Kalatehjari, R., Brook, M.S. (2025) Evolution and critical evaluation of deterministic physically based rainfall-induced landslide susceptibility mapping: a mixed review. *Nat Hazards* 121, 20795–20818. https://doi.org/10.1007/s11069-025-07634-0

Saha, A., Villuri, V.G.K., Bhardwaj, A. (2024) Exploring machine learning and statistical approach techniques for landslide susceptibility mapping in Siwalik Himalayan region using geospatial technology. *Environ Sci Pollut Res* 31, 10443–10459. https://doi.org/10.1007/s11356-023-31670-7

Selamat, S.N., Majid, N.A. & Taha, M.R. Multicollinearity and spatial correlation analysis of landslide conditioning factors in Langat River Basin, Selangor. Nat Hazards 121, 2665–2684 (2025). https://doi.org/10.1007/s11069-024-06903-8

Shannon, C.E. (1948) A mathematical theory of communication. *Bell Syst Tech J* 27, 379–423. https://doi.org/10.1002/j.1538-7305.1948.tb01338.x

Wendim, S., Mebrahtu, G., Woldearegay, K. (2025) GIS-based landslide susceptibility mapping using Analytical Hierarchy Process method along Gedo-Dilb asphalt road section, Northern Ethiopia. *Bull Eng Geol Environ* 84, 440. https://doi.org/10.1007/s10064-025-04455-0

Wilson, J.P., Gallant, J.C. (2000) *Terrain analysis: principles and applications*. John Wiley & Sons, New York.

Wooldridge, J.M. (2015) *Introductory Econometrics: A Modern Approach*, 6th ed. Cengage Learning, Boston.

Yilmaz, I. (2009) Landslide susceptibility mapping using frequency ratio, logistic regression, artificial neural networks and their comparison: a case study from Kat landslides (Tokat–Turkey). *Comput Geosci* 35, 1125–1138. https://doi.org/10.1016/j.cageo.2008.08.007

Yilmaz, O.S. (2022) Flood hazard susceptibility areas mapping using Analytical Hierarchical Process (AHP), Frequency Ratio (FR) and AHP-FR ensemble based on Geographic Information Systems (GIS): a case study for Kastamonu, Türkiye. *Acta Geophys* 70, 2747–2769. https://doi.org/10.1007/s11600-022-00882-9

Youssef, A.M., Pourghasemi, H.R. (2020) Landslide susceptibility mapping using machine learning algorithms and comparison of their performance at Abha Basin, Asir Region, Saudi Arabia. *Geosci Front* https://doi.org/10.1016/j.gsf.2020.05.010

Zhao, H., Yao, L., Mei, G., Liu, T., Ning, Y. (2017) A fuzzy comprehensive evaluation method based on AHP and entropy for a landslide susceptibility map. *Entropy* 19(8), 396. https://doi.org/10.3390/e19080396

Zighmi, K., Zahri, F., Faqeih, K., Al, A.A., Riheb, H., Alamri, S.M., Alamery, E. (2025) AHP multi criteria analysis for landslide susceptibility mapping in the Tellian Atlas chain. *Sci Rep* 15, 25747. https://doi.org/10.1038/s41598-025-10819-z

Declarations

Acknowledgments The authors would like to thank the anonymous reviewers for their valuable comments, which improved the manuscript. They also acknowledge all data providers and tool developers whose contributions are duly cited in the main manuscript.

Funding The authors declare that no funds, grants, or other support was received during the preparation of this manuscript.

Author contributions Pang Hyon-Ryong contributed to study conception and design. Material preparation and field work were performed by Jang Chol-Ju and Paek Chung-Hyok, and data collection and analysis were performed by Ri Ryong-Kil, Jang Chol-Ju, Ri Hyok, Choe Yun-Chol and Jon Kyong-Ho. The first and final draft of the manuscript was written by Pang Hyon-Ryong.

Ethical Approval* This is not applicable

Consent to Participate* This is not applicable.

Consent to Publish* This is not applicable

Competing interests The authors have no relevant financial or nonfinancial interests to disclose.

Data availability statement All the data generated or analyzed during this study are included in this published article. For additional data requests, please contact the corresponding author, who will provide access upon request.